



HAL
open science

3D Modeling of satellite spectral images, radiation budget and energy budget of urban landscapes

Jean-Philippe Gastellu-Etchegorry

► **To cite this version:**

Jean-Philippe Gastellu-Etchegorry. 3D Modeling of satellite spectral images, radiation budget and energy budget of urban landscapes. *Meteorology and Atmospheric Physics*, 2008, MAP-0/939, pp.1-21. 10.1007/s00703-008-0344-1 . ird-00405362

HAL Id: ird-00405362

<https://ird.hal.science/ird-00405362v1>

Submitted on 20 Jul 2009

HAL is a multi-disciplinary open access archive for the deposit and dissemination of scientific research documents, whether they are published or not. The documents may come from teaching and research institutions in France or abroad, or from public or private research centers.

L'archive ouverte pluridisciplinaire **HAL**, est destinée au dépôt et à la diffusion de documents scientifiques de niveau recherche, publiés ou non, émanant des établissements d'enseignement et de recherche français ou étrangers, des laboratoires publics ou privés.

Centre d'Etudes Spatiales de la Biosphère Paul Sabatier University,
CNES – CNRS, IRD, Toulouse Cedex, France

3D Modeling of satellite spectral images, radiation budget and energy budget of urban landscapes

J. P. Gastellu-Etchegorry

With 15 Figures

Received 16 April 2007; Accepted 27 October 2008
Published online • • 2008 © Springer-Verlag 2008

15 Summary

16 DART EB is a model that is being developed for simulating
17 the 3D (3 dimensional) energy budget of urban and natural
18 scenes, possibly with topography and atmosphere. It simu-
19 lates all non radiative energy mechanisms (heat conduction,
20 turbulent momentum and heat fluxes, water reservoir evo-
21 lution, etc.). It uses DART model (Discrete Anisotropic
22 Radiative Transfer) for simulating radiative mechanisms:
23 3D radiative budget of 3D scenes and their remote sensing
24 images expressed in terms of reflectance or brightness tem-
25 perature values, for any atmosphere, wavelength, sun/view
26 direction, altitude and spatial resolution. It uses an innova-
27 tive multispectral approach (ray tracing, exact kernel, dis-
28 crete ordinate techniques) over the whole optical domain.

29 This paper presents two major and recent improvements of
30 DART for adapting it to urban canopies. (1) Simulation of
31 the geometry and optical characteristics of urban elements
32 (houses, etc.). (2) Modeling of thermal infrared emission by
33 vegetation and urban elements. The new DART> version
34 was used in the context of the CAPITOUL project. For that,
35 districts of the Toulouse urban data base (Autocad format)
36 were translated into DART scenes. This allowed us to
37 simulate visible, near infrared and thermal infrared satellite
38 images of Toulouse districts. Moreover, the 3D radiation
39 budget was used by DARTEB for simulating the time evo-
40 lution of a number of geophysical quantities of various sur-
41 face elements (roads, walls, roofs). Results were successfully

compared with ground measurements of the CAPITOUL 42
project. 43

1. Introduction 44

Modeling the radiative behavior and the energy 45
budget of terrestrial surfaces is relevant for many 46
scientific domains. It is typically the case for 47
studying vegetation functioning with remotely 48
acquired information. For example, the albedo 49
of a canopy with an anisotropic Bidirectional 50
Reflectance Factors (BRF) may be underesti- 51
mated by as much as 45% if it is computed with 52
nadir reflectance only (Kimes and Sellers 1985). 53
Radiative transfer models have the potential for 54
correcting this type of error. However, in order to 55
be efficient tools, models must account for the 56
three dimensional (3D) nature of Earth surfaces. 57
Neglect of the 3D structure of canopies can lead 58
to errors on the 3D radiation budget and remote 59
sensing measurements. For example, it can 60
lead to errors on vegetation BRF and direc- 61
tional brightness temperature (DTDF) distribu- 62
tion functions as large as 50%, depending on 63
instrumental (e.g., view and sun directions) and 64
experimental (e.g., vegetation heterogeneity) con- 65
ditions (Gastellu-Etchegorry et al. 1999). The 66
problem is similar for urban canopies due to their 67

Correspondence: Jean Philippe Gastellu-Etchegorry, Centre
d'Etudes Spatiales de la Biosphère Paul Sabatier University,
CNES – CNRS, IRD 18 avenue Edouard Belin, BPi 2801, 31401
Toulouse Cedex 4, France (E-mail: gastellu@cesbio.cnes.fr)

1 strong spatial heterogeneity. The application of
 2 radiative transfer modeling to urban surfaces is
 3 important in the context of the advent of satellite
 4 sensors with spatial and spectral resolutions that
 5 are more and more adapted to urban characteris-
 6 tics such as building dimensions and temperature
 7 spatial variability. It explains the numerous works
 8 conducted in the field of remote sensing of urban
 9 surfaces (Voogt and Oke 1998; Soux et al. 2004).
 10 The use of descriptions with qualitatively based
 11 land use data instead of more fundamental surface
 12 descriptors is a source of inaccuracy for modeling
 13 BRFs and DTDFs (Voogt and Oke 2003).

14 These remarks stress the usefulness of 3D ra-
 15 diative transfer models. The DART (Discrete
 16 Anisotropic Radiative Transfer) model (Gastellu-
 17 Etchegorry et al. 1996) was developed in this
 18 context for simulating remote sensing images
 19 of 3D vegetation canopies in the visible/near in-
 20 frared (NIR) spectral domain. However, it did
 21 not model thermal infrared (TIR) emission and
 22 could not operate with urban landscapes. After a
 23 brief introduction of DART, this paper presents
 24 two major and recent improvements that allow
 25 DART to operate on urban landscapes, possibly
 26 with vegetation, topography, atmosphere, and at-
 27 mospheric turbidity within the scene, over the
 28 whole optical domain. (1) Simulation of the geo-
 29 metry and optical characteristics of urban elements
 30 (houses, etc.). (2) Modeling of TIR emission by
 31 vegetation and urban elements. As a result, the
 32 present DART model simulates the radiation bud-
 33 get and remote sensing images of natural and ur-
 34 ban canopies, for any experimental (sun direction,
 35 canopy heterogeneity, topography, more or less
 36 turbid atmosphere, etc.) and instrumental (view
 37 direction, spatial resolution, etc.) configuration.

38 The last part of the paper presents results ob-
 39 tained in the context of the CAPITOU project,
 40 thanks to the above mentioned improvements.
 41 Firstly, visible, NIR and TIR satellite images of
 42 Toulouse districts are shown. They were obtained
 43 with DART scenes that were directly derived
 44 from the Toulouse urban data base (Autocad for-
 45 mat). Secondly, an extension of the DART mod-
 46 el, called DARTEB (DART energy budget), that
 47 is being developed for simulating the 3D energy
 48 budget of vegetation and urban canopies is pres-
 49 ented. Finally, preliminary results from DARTEB
 50 are compared with ground measurements of the
 51 CAPITOU project.

2. DART model

52

DART was originally developed for simulating
 BRFs, remote sensing images and the spectral
 radiation budget of 3D natural (e.g., trees, roads,
 grass, soil, water) landscapes in the visible and
 short wave infrared domains. Since its first re-
 lease in 1996, it was successfully tested, in the
 case of vegetation canopies, against reflectance
 measurements (Gastellu-Etchegorry et al. 1999)
 and against a number of 3-D reflectance models
 (e.g., *Flight* (North 1996), *Sprint* (Thompson and
 Goel 1998), *Raytran* (Govaerts and Verstraete
 1998)), in the context of the RAMI (RADIATION
 transfer Model Intercomparison) experiment
 (Pinty et al. 2001, 2004; Widlowski et al. 2007,
 2008). Only BRFs could be compared because
 DART is the only 3-D model that simulates
 images.

DART was successfully used in many scientific
 domains: impact of canopy structure on satellite
 images texture (Pinel and Gastellu-Etchegorry
 1998) and reflectance (Gastellu-Etchegorry et al.
 1999), 3D distribution of photosynthesis and pri-
 mary production rates of vegetation canopies
 (Guillevic and Gastellu-Etchegorry 1999), in-
 fluence of Norway forest spruce structure and
 woody elements on LAI retrieval (Malenovský
 et al. 2005) and canopy reflectance (Malenovský
 et al. 2008), determination of a new hyperspectral
 index for chlorophyll estimation of forest canopy
 (Malenovský et al. 2006), etc.

DART simulates radiative transfer in heteroge-
 neous 3-D landscapes with the exact kernel and
 discrete ordinate methods. It uses an iterative ap-
 proach: radiation intercepted in iteration “*i*” is
 scattered in iteration “*i* + 1”. Any landscape is
 simulated as a rectangular matrix of parallelepi-
 pedic cells. Figure 1 illustrates the way urban and
 natural landscapes are simulated, possibly with
 topography and atmosphere. The atmosphere is
 made of cells the size of which increases with
 altitude. Radiation is restricted to propagate in
 a finite number of directions (Ω_i) with an angular
 sector width ($\Delta\Omega_i$) (sr). Any set of N discrete
 directions can be selected ($\sum_{n=1}^N \Delta\Omega_n = 4\pi$).
 A radiation that propagates along direction (Ω_i)
 at a position r is called a source vector $W(r, \Omega_i)$.
 It has 3 components: total radiation W , radiation
 unrelated to leaf mesophyll and polarization de-
 gree associated to first order scattering.

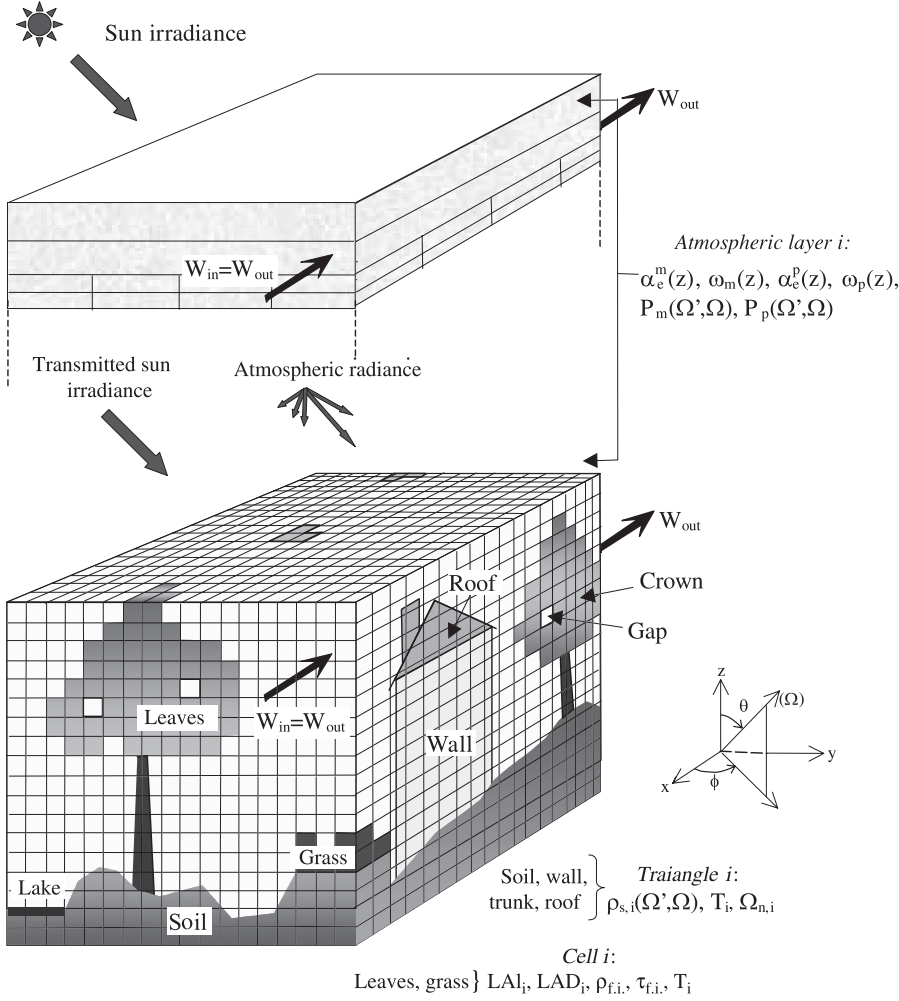


Fig. 1. “Atmosphere + Earth” simulation used as an input to DART model. It shows a mixed “built-up/natural Earth landscape + atmosphere”

1 The number of possible ray paths is finite be-
 2 cause the number of directions is finite and be-
 3 cause within each DART cell, the origin of any
 4 ray is a point P among the N_{sc}^3 points that sample
 5 the cell or the $6 \cdot N_{sf}^2$ points that sample the 6 cell
 6 faces. Thus, there are $(N_{sc}^3 + 6 \cdot N_{sf}^2)$ paths for
 7 each discrete direction, with $N_{sf} = N_{sc}$ for scatter-
 8 ing mechanisms, and $N_{sf} = 2 \cdot N_{sc}$ for emission
 9 mechanisms, usually with $N_{sc} = 7$. In a first step,
 10 DART computes the $(N_{sc}^3 + 6 \cdot N_{sf}^2)$ possible
 11 paths from cell $(0, 0, 0)$. This pre-computation
 12 eliminates unnecessary repetitive computations
 13 during the tracking of source vectors because it
 14 allows a simple calculation of any ray path from
 15 any cell: the coordinates of the i th cell encoun-
 16 tered by a source vector that propagates within
 17 the scene are the coordinates of the cell where it
 18 originates plus the i th coordinates of the pre-
 19 computed ray path that has the same direction.

20 Scene irradiance has 2 components: direct sun
 21 $W(\Omega_s)$ and atmospheric $W_a(\Omega_n)$ source vectors.

$W(\Omega_s)$ propagates along direction (Ω_s) . $W(\Omega_s)$ 22
 and $W_a(\Omega_n)$ are simulated from a fictitious cell 23
 layer on top of the scene (Fig. 1), with values 24
 equal to: 25

$$W(\Omega_s) = E_s(\Omega_s) \cdot |\mu_s| \cdot \Delta x \cdot \Delta y$$

$$W_a(\Omega_n) = L_a(\Omega_n) \cdot |\mu_n| \cdot \Delta x \cdot \Delta y \cdot \Delta \Omega_n$$

where $\Delta x \cdot \Delta y$ is the area of the cell face, $\mu_s =$ 27
 $\cos \theta_s$, $\mu_n = \cos \theta_n$, $E_s(\Omega_s)$ is the solar con- 28
 stant at the top of the scene, and Ω_s denotes 29
 the solar incident direction. $L_a(\Omega_n)$ is the atmo- 30
 spheric radiance along direction (Ω_n) , with 31
 $n \in [1 N']$, where N' is the number of downward 32
 discrete directions. It is null at the top of the 33
 atmosphere. 34

35 Generally speaking, two types of radiation in-
 36 teraction take place. (1) Volume interaction with-
 37 in turbid cells the juxtaposition of which is used
 38 to simulate vegetation elements. (2) Surface in-
 39 teraction on triangles the juxtaposition of which
 40 is used to simulate urban surfaces and topogra-

1 phy. Radiation interaction within turbid cells is
 2 described in Gastellu-Etchegorry et al. (2004).
 3 Within cell first order scattering is exactly com-
 4 puted. As expected, simplifying hypotheses are
 5 used for simulating multiple scattering. It is
 6 now computed with a much faster approach
 7 than the initial “harmonic expansion approach:
 8 it is computed using the energy intercepted with-
 9 in a finite number of incident angular sectors
 10 $\Omega_{\text{sect},k}$ that sample the 4π space of directions
 11 ($\sum \Omega_{\text{sect},k} = 4\pi$). The number of sectors can be
 12 as large as the number of directions of ray prop-
 13 agation, but a number equal to 6 leads to very
 14 accurate results, with relative errors smaller than
 15 10^{-3} (Gastellu-Etchegorry et al. 2004). Another
 16 major improvement concerns scattering by turbid
 17 cells. Now, scattered radiation starts from a point
 18 $M_s(z_{m\uparrow})$ for upward directions (Ω_v) and a point
 19 $M_s(z_{m\downarrow})$ for downward directions (Ω_v). The alti-
 20 tudes $z_{m\uparrow}$ and $z_{m\downarrow}$ are those that give exact results
 21 for two specific upward $\Omega_{m\uparrow}$ and downward $\Omega_{m\downarrow}$
 22 directions in the case of homogeneous turbid me-
 23 dia. Optimal values are $\theta_{m\uparrow} = 20^\circ$ and $\theta_{m\downarrow} = 160^\circ$.
 24 These points are computed for each cell face
 25 $f (f \in [1, 6])$ that intercepts incident rays, and for
 26 each angular sector “incident” on the cell face
 27 (Martin 2006). This implies that intercepted vec-
 28 tor sources $W_{\text{int}}(f, \Omega_{\text{sect},k})$ are stored per cell face
 29 f and per incident angular sector $\Omega_{\text{sect},k}$.

30 Thus:

$$W_{\text{int}}(f, \Omega_{\text{sect},k}) = \sum_{\Omega_s} W_{\text{int}}(f, \Omega_s),$$

32 with directions (Ω_s) within ($\Omega_{\text{sect},k}$). For the case
 33 “direct sun illumination”, there is only 1 sector.

34 Atmospheric radiative transfer modeling is im-
 35 plemented for any spectral band in the optical
 36 domain from the ultraviolet up to the thermal
 37 infrared (Dallest 2001; Gascon 2001). It simu-
 38 lates the atmospheric backscattering phenome-
 39 non, which avoids the need to couple DART
 40 with an atmospheric model. Atmospheric optical
 41 properties are characterized by the molecular
 42 $P_m(\lambda, \Omega', \Omega)$ and aerosol $P_p(\lambda, \Omega', \Omega)$ phase func-
 43 tions and by a number of profiles (molecular ex-
 44 tinction coefficient $\alpha_e^m(\lambda, z)$ and spherical albedo
 45 $\omega_m(\lambda, z)$, aerosol extinction coefficient $\alpha_e^p(\lambda, z)$
 46 and spherical albedo $\omega_p(\lambda, z)$). These quantities
 47 are specified by the operator or come from a data
 48 base ($[0.3 \mu\text{m} - 30 \mu\text{m}]$) pre-computed with the
 49 Modtran atmospheric model (Berk et al. 1989),
 50 for a few predefined atmospheres. DART atmo-

spheric reflectance, transmittance and brightness
 temperature are very close to Modtran simula-
 tions in the case of lambertian horizontal Earth
 surfaces (Grau 2008).

Images are simulated in the focal plane of the
 satellite sensor (Gentine 2002) with the steps:

- Projection of upward source vectors onto an
oversampled horizontal grid on top the scene
simulation. The cross section of the emitters
and scatterers at the origin of the signal is
used for improving the geometric accuracy of
images, especially for scenes with marked 3D
architectures (urban elements, topography).
- Bi-linear interpolation method that projects
the horizontal upper grid of the scene onto
an over sampled grid in the sensor plane, at
any altitude (bottom to top of the atmosphere).
- Signal convolution with sensor spectral
characteristics.

DART works with a specifically designed
 Graphic User Interface (GUI) for imputing para-
 meters that characterize the landscape and the
 view and illumination conditions.

3. Simulation of urban elements

Urban elements (e.g., roads, wall, roof) are sim-
 ulated as the juxtaposition of parallelograms
 and triangles, hereafter called “opaque figures”.
 Opaque figures are also used for simulating to-
 pography. As a result, DART cells can be empty
 or filled with either turbid media or plane sur-
 faces. Although all opaque figures undergo the
 same radiative mechanisms, cells that contain
 opaque figures (Fig. 2) belong to different cell
 types (e.g., roof and wall cells) for differentiating
 their radiation budget. This is used also for
 obtaining realistic scene displays. The type of a
 cell that contains all or part of an opaque figure is
 the type of that opaque figure. Figure 2 shows the

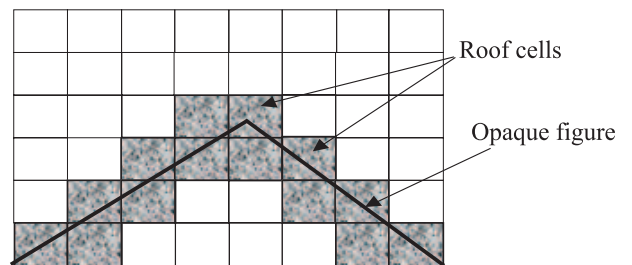


Fig. 2. Cells “Roof” and opaque figures

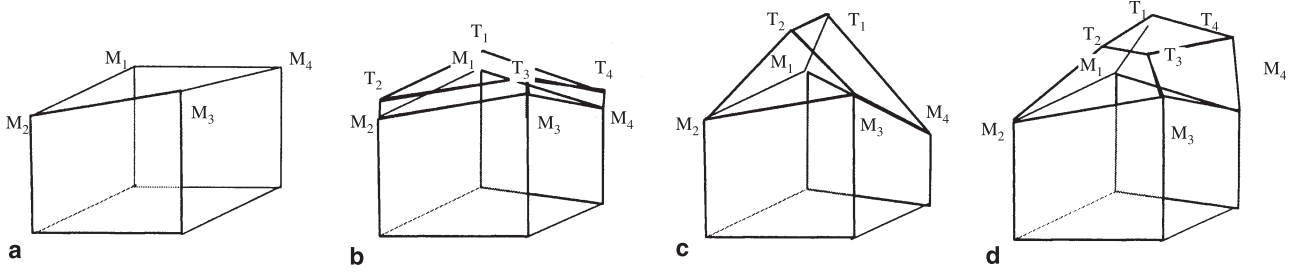


Fig. 3. The 4 pre-defined house types. (a) No roof. (b) Plate. (c) Classic. (d) Complex

- 1 intersection of cells with 2 opaque figures that
 2 simulate a roof. These cells are called *Roof cells*.
 3 Actually, cells can contain or be intersected by
 4 several figures. The type of a cell crossed by
 5 figures that belong to different urban elements
 6 (e.g., roof + wall) is the type of the last simulated
 7 urban element.
 8 From the radiative transfer point of view,
 9 buildings can have very complex shapes. They
 10 are the superimposition of generic volume ele-
 11 ments (e.g., tetrahedron, pyramid, column, chim-
 12 ney, etc) defined by any 8 points and 6 faces.
 13 Urban canopy simulation is eased with the pre-
 14 definition of four major urban elements:
- 15 • *Small wall*: it is defined by its 4 upper corners
 16 and its optical properties.
 - 17 • *House*: it is made of 2 elements (4 walls + 1
 18 roof) simulated by a generic model.
 - 19 – The 4 walls are defined by their optical
 20 properties and their 4 upper corners (x, y, z).
 - 21 – The roof. Its 4 lower points are the 4 upper
 22 corners of the walls, whereas its top is de-
 23 fined by 0 to 4 points, depending on the type
 24 of roof (Fig. 3).
 - 25 * No roof. The roof is made of 2 triangles
 that link the top corners of the walls
 (Fig. 3a).
 - * Plate. The roof is a layer defined by a verti-
 cal shift (roof depth) from the 4 top wall
 corners (x, y, z), which defines the 4 points
 T_1, T_2, T_3 and T_4 of the roof (Fig. 3b).
 - * Classic. The roof is defined by the 2 up-
 per points T_1, T_2 of the roof (Fig. 3c).
 - * Complex. The roof is defined by the 4
 upper points T_1, T_2 of the roof (Fig. 3d).
- 36 • *Building*: set of houses with identical optical
 37 properties for their walls and roofs.
 - 38 • *Road*: defined by its width and the coordinates
 39 (x, y) of the projection of consecutive points

onto a horizontal plane. The associated seg- 40
 ments define the cells called *Route*. 41

Any radiation scattered $W_{\text{scat}}(\Omega_v)$ by an opa- 42
 que surface of reflectance $\rho(\Omega_s, \Omega_v)$ is the prod- 43
 uct of the incident vector source $W_{\text{in}}(\Omega_s)$ by 44
 the transfer function $T(\Omega_s, \Omega_v)$, which depends 45
 on $\rho(\Omega_s, \Omega_v)$. There are 4 possible types of 46
 reflectance: 47

- *Type 0*: “Lambertian + random spatial vari- 48
 ability”. 49
- *Type 1*: “Lambertian + specular reflectance 50
 $\rho_{\text{spec}}(\Omega_s, \Omega_v)$ ”. 51
- *Type 2*: “Hapke + specular”. 52
- *Type 3*: Pre-computed functions $T_d(\Omega_s, \Omega_v)$, 53
 $T_{\text{spe}}(\Omega_s, \Omega_v)$ and $T_{\text{pol}}(\Omega_s, \Omega_v)$ 54

These 4 types of reflectance and the associated 55
 physical laws are presented in the Annex. 56

Vegetation elements are simulated as the jux- 57
 taposition of turbid cells. These cells contain a 58
 turbid medium made of infinitesimal planar ele- 59
 ments that are characterized by specific optical 60
 properties (reflectance, transmittance), a statisti- 61
 cal distribution of orientations (LAD: Leaf Angle 62
 Distribution) and a surface density (LAI: Leaf 63
 Area Index). 64

4. Ray tracking in presence of opaque figures 65

Surface scattering and emission mechanisms as- 66
 sociated with urban elements are modeled using 67
 surface optical properties introduced in the pre- 68
 vious chapter. The radiation scattered and/or 69
 emitted by opaque figures can be intercepted by 70
 other scene elements (i.e., turbid medium or opa- 71
 que element) within the cell itself and/or other 72
 cells (Gastellu-Etchegorry 2007). Approaches 73
 adopted for managing ray interception by opaque 74
 figures, for determining the origins of rays that 75
 are scattered and emitted by opaque figures, and 76

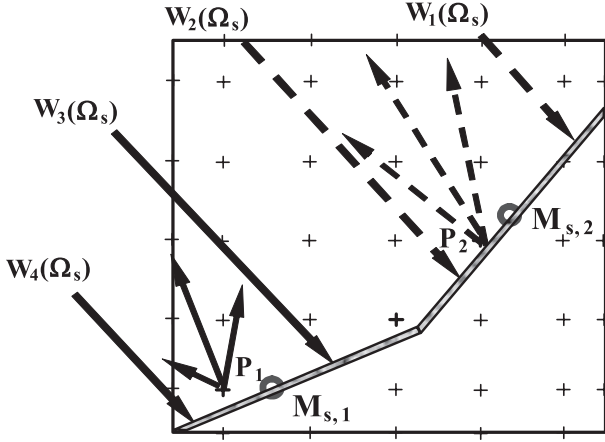


Fig. 4. Interception of 4 rays by 2 figures. W_1 and W_2 are intercepted by Fig. 2. W_3 and W_4 are intercepted by Fig. 1. Resulting effective points of emission are P_2 and P_1

- 1 for tracking rays in presence of opaque figures
- 2 are presented below.

3 4.1 Radiation interception by an opaque figure

4 The within cell interaction “ray – figures (i.e.,
5 triangle/parallelogram)” is modeled in 2 steps:

6 1) Determination if the ray (i.e., $W_1(\Omega_s)$,
7 $W_2(\Omega_s)$, $W_3(\Omega_s)$, $W_4(\Omega_s)$ in Fig. 4) incident
8 on the cell intercepts the plane {point, normal
9 vector} that contains every figure in the cell.

10 2) If there is a point of interception (M), it is
11 checked if this point is both in the cell and
12 in the figure. A test on the co-ordinates of (M)
13 indicates if this point belongs or not to the
14 cell. Two steps allow one to determine if
15 (M) belongs to the figure:

- 16 (i) Change of reference to express the co-ordi-
nates of M in the reference of the figure.
- 17 (ii) These co-ordinates are submitted to N
inequations, associated to N constraints,
18 N being the number of edges of the figure.

21 4.2 Origin of radiation scattered/emitted 22 by an opaque figure

23 Rays are scattered and emitted from $(N_{sc}^3 +$
24 $6 \cdot N_{sf}^2)$ predefined points. The determination of
25 these points is carried out in 2 stages:

- 26 1) For each intercepting figure, a barycentric
27 method computes the exact emission point:
28 if a ray intersects a figure in a cell, the new

exact emission point of the figure is the ener- 29
gy barycentre of this intersection point and 30
the exact emission point, calculated before 31
this intersection (e.g., $M_{s,1}$ and $M_{s,2}$ in Fig. 32
4). This point is always on the figure. 33

- 2) Determination of the effective point of emis- 34
sion (e.g., P_1 and P_2 in Fig. 4) among the 35
 $(N_{sc}^3 + 6 \cdot N_{sf}^2)$ points which sample the cell. 36
The center (called “sub-center”) of the sub- 37
cell that contains (M_{si}) is the first guess. It is 38
determined by thresholding the co-ordinates 39
of (M_{si}). If it is not acceptable, another point 40
is searched for. In order to be accepted, a 41
point P_i must be as close as possible of 42
(M_{si}) and must verify: 43

- a) (P_i) is outside the volume bounded by the 44
emitting figure. 45
- b) there is no figure between (P_i) and (M_{si}). 46

The search of the effective point P_i uses a 47
test on the directions of vectors “sub-center → 48
figure” and “perpendicular of the figure”. If 49
these directions are: 50

- not opposed (i.e., cosine < 0), with no figure 51
between (M_{si}) and (P_i): (P_i) is accepted. 52
- opposite: (P_i) is shifted with a sub-grid shift 53
($\pm \Delta X/N$, $\pm \Delta Y/N$ or $\pm \Delta Z/N$) along the axis 54
(Ox , Oy or Oz) for which the absolute value of 55
the component in X , Y or Z of the normal vec- 56
tor to the figure is largest. ΔX , ΔY , ΔZ are the 57
cell dimensions. 58

If no point (P_i) is found both within the cell 59
and outside the scene element bounded by the 60
figure, (P_i) is searched in a systematic way 61
among all possible $(N_{sc}^3 + 6 \cdot N_{sf}^2)$ points (P_i) of 62
the cell, starting from closer centers. If no point 63
is found, energy is lost and stored in a variable. 64
Actually, this energy loss is always negligible. 65

4.3 Ray tracking from an opaque figure 66

The interest of effective points of emission (P_i) 67
is that all possible paths that start from them are 68
pre-calculated. The actual path of any ray that 69
comes from a point (P_i) of the cell is pre-cal- 70
culated as far as the intersection point (Q) of the ray 71
with the horizontal plane that contains the upper 72
or bottom face of the cell. Then, the ray follows 73
the pre-calculated path which originates in the 74
closer sub-center (E_i) of the horizontal plane. 75

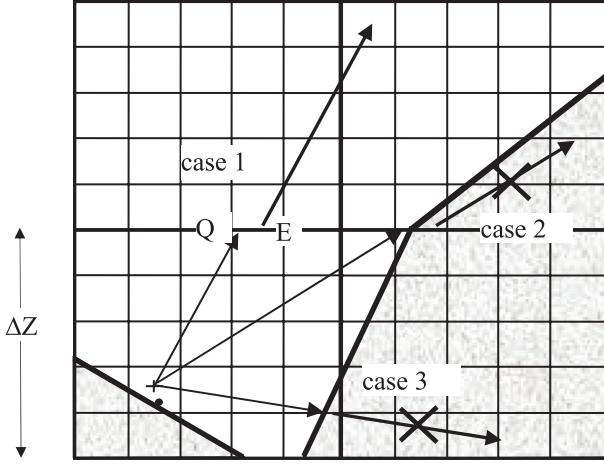


Fig. 5. Illustration of ray tracking in presence of opaque figures

- 1 Figure 5 illustrates some cases that occur during
 2 ray tracking in presence of opaque figures.
- 3 • *Case 1:* Occurrence of a small geometrical
 4 shift between the points (Q_i) and (E_i).
- 5 • *Case 2:* The ray goes under the figure in the
 6 following cell. If the segment ($Q_i E_i$) intersects
 7 a figure, the energy of the ray is stored on the
 8 first intersected figure.
- 9 • *Case 3:* The ray intersects a figure in the cell.
 10 If the segment ($Q_i E_i$) intersects a figure of the
 11 cell, the energy of the ray is attributed to the
 12 closest intercepted figure.

13 5. Modeling emission mechanisms

14 TIR modeling was introduced by Boyat (2001)
 15 and Guillevic et al. (2003) with methods (i.e.,

discrete ordinate and exact kernel methods, 16
 etc.) similar to those used for tracking visible 17
 and NIR radiation. Major recent improvements 18
 are presented below. 19

5.1 Thermal emission of leaf turbid cells 20

Compared to radiative transfer modeling in the 21
 short wavelengths, a major specificity of TIR 22
 modeling is the emission of turbid leaf cells. In- 23
 deed, it is calculated on a cell per cell basis as the 24
 integration of the Planck law over a specified 25
 spectral band. 26

• Theoretical approach 27

Let us consider the radiation $dW_{ij}(\lambda, \Omega_v, T)$ 28
 that a cell emits along direction Ω_v , through 29
 a surface element S_{ij} of face k of the cell 30
 (Fig. 6). The emission comes from the cell vol- 31
 ume $V(k, \Omega_v)$. 32

We have: 33

$$dW_{ij}(\lambda, \Omega_v, T) = L_{B,f}(\lambda, T) \cdot G(\Omega_v) \cdot u_f \cdot \Delta\Omega_v \cdot \int_{V(k, \Omega_v)} \exp[-G(\Omega_v) \cdot u_f \cdot \Delta l(dV)] \cdot dV$$

$$dW_{ij}(\lambda, \Omega_v, T) = L_{B,f}(\lambda, T) \cdot \cos(\Psi_{nv}) \cdot \Delta\Omega_v \cdot \{1 - \exp[-G(\Omega_v) \cdot u_f \cdot L_{ij}]\} \cdot S_{ij}$$

$L_{B,f}(\lambda, T) = \varepsilon_{f,t} \cdot L_B(\lambda, T)$: radiance of a leaf 35
 with temperature T , at wavelength λ . 36

Ψ_{nv} : angle between direction Ω_v and the normal 37
 Ω_n of the face. 38

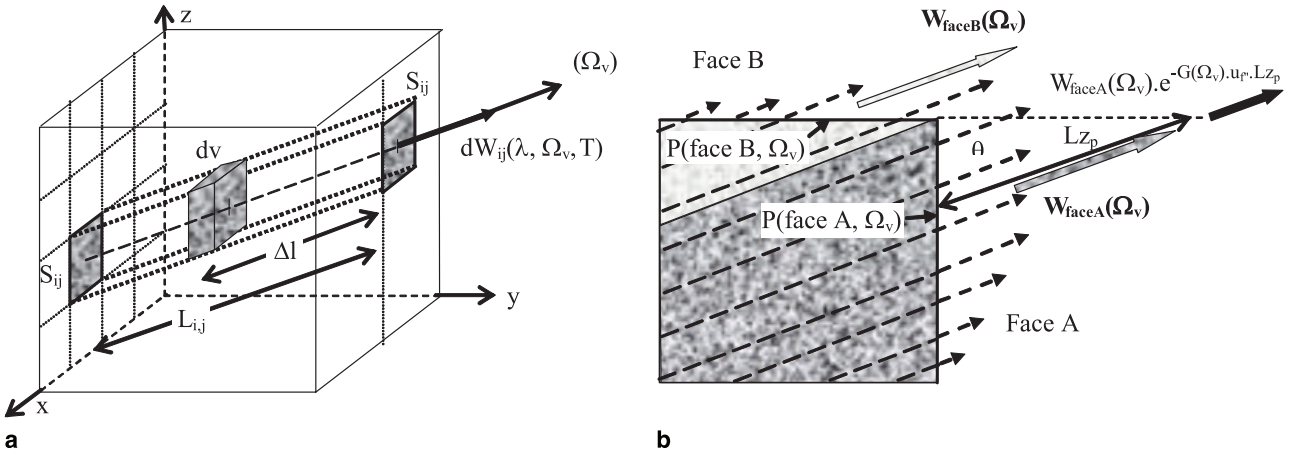


Fig. 6. Computation of the TIR emission of a turbid cell (T, u_f, LAD)

1 Thus, the total emitted energy that crosses face
2 k is:

$$\begin{aligned} W_{1 \text{ face } k}(\Omega_v) &= \sum_{ij} dW_{ij}(\Omega_v) \\ &= L_{B,f}(\lambda, T) \cdot \cos(\Psi_{nv}) \cdot \Delta\Omega_v \\ &\quad \cdot \sum_{ij} \{1 - \exp[-G(\Omega_v) \cdot u_f \cdot L_{ij}]\} \cdot S_{ij} \end{aligned}$$

4 If there are \mathcal{T} leaf species ($u_{f,t}, T_t, G_t(\Omega_v)$), with
5 $t \in [1 \mathcal{T}]$, the total emission through face k is:

$$\begin{aligned} W_{1 \text{ face } k}(\Omega_v) &= \frac{\sum_t L_{B,f}(\lambda, T_t) \cdot G_t(\Omega_v) \cdot u_{f,t} \cdot \cos(\Psi_{nv}) \cdot \Delta\Omega_v}{\sum_t G_t(\Omega_v) \cdot u_{f,t}} \\ &\quad \cdot \sum_{ij} \left\{ 1 - \exp \left[- \sum_t G_t(\Omega_v) \cdot u_{f,t} \cdot L_{ij} \right] \right\} \cdot S_{ij} \end{aligned}$$

7 Source vector $dW_{ij}(\lambda, \Omega_v, T)$ that escapes sur-
8 face S_{ij} along direction (Ω_v) is the sum of the
9 energy emitted by all volume elements dv within
10 volume $S_{ij} \times L_{ij}$. Total energy emitted along (Ω_v)
11 comes from 1 up to 3 cell faces depending on (Ω_v).

12 • Within cell scattering

13 Part of the TIR emission is intercepted before
14 exiting the cell, which leads to scattering of order
15 1 and larger.

16 Thus, the energy intercepted along the direc-
17 tion (Ω_v) is:

$$\begin{aligned} W_{\text{int}}(\lambda, \Omega_v, T) &= L_{B,f}(\lambda, T) \cdot G(\Omega_v) \cdot u_f \cdot \Delta\Omega_v \\ &\quad \cdot \left\{ V_{\text{cell}} - \frac{\cos \Psi_{nv}}{G(\Omega_v) \cdot u_f} \right. \\ &\quad \left. \cdot \sum_k \sum_{ij} [1 - e^{-G(\Omega_v) \cdot u_f \cdot L_{ij}}] \cdot S_{ij} \right\} \end{aligned}$$

19 With \mathcal{T} leaf species ($u_{f,t}, T_t, G_t(\Omega_v)$) and $t \in$
20 $[1 \mathcal{T}]$, total energy intercepted along (Ω_v) is:

$$\begin{aligned} W_{\text{int}}(\lambda, \Omega_v, T) &= \sum_t L_{B,f}(\lambda, T_t) \cdot G_t(\Omega_v) \cdot u_{f,t} \cdot \Delta\Omega_v \\ &\quad \cdot \left\{ V_{\text{cell}} - \frac{\cos \Psi_{nv}}{\sum_t G_t(\Omega_v) \cdot u_{f,t}} \right. \\ &\quad \left. \cdot \sum_k \sum_{ij} [1 - e^{-\sum_t G_t(\Omega_v) \cdot u_{f,t} \cdot L_{ij}}] \cdot S_{ij} \right\} \end{aligned}$$

22 Total interception is:

$$W_{\text{int}}(\lambda, T) = \sum_{v=1}^{N_{\text{dir}}} W_{\text{int}}(\lambda, \Omega_v, T)$$

Scattering radiation that exits the cell is simu- 24
lated as a geometric series: 25

$$\begin{aligned} W_M(\lambda, T) &= W_{\text{int}}(\lambda, T) \cdot \{ \omega_\lambda \cdot \langle T \rangle \\ &\quad + \omega_\lambda \cdot \langle T \rangle \cdot [\omega_\lambda - \omega_\lambda \cdot \langle T \rangle] \\ &\quad + \omega_\lambda \cdot \langle T \rangle \cdot [\omega_\lambda - \omega_\lambda \cdot \langle T \rangle]^2 + \dots \} \\ W_M(\lambda, T) &= \left[\frac{\omega_\lambda \cdot \langle T \rangle}{1 - \omega_\lambda \cdot [1 - \langle T \rangle]} \right] \cdot W_{\text{int}}(\lambda, T) \end{aligned}$$

with $\langle T \rangle$ = mean transmittance on all N_{dir} direc- 27
tions from cell center: 28

$$\langle T \rangle = \frac{1}{4\pi} \cdot \int_{4\pi} e^{-G(\Omega) \cdot u_f \cdot \Delta m(\Omega)} \cdot d\Omega$$

where $\Delta m(\Omega_v)$ = path along (Ω_v) from the cell 30
center to the exit cell face. 31

With \mathcal{T} leaf species 32

$$\begin{aligned} (u_{f,t}, T_t, G_t(\Omega_v)): \omega &= \frac{\sum_t \omega_{f,t} \cdot u_{f,t}}{\sum_t u_{f,t}}, \quad \langle T \rangle = \Pi_t \langle T \rangle_t, \\ G(\Omega_v) \cdot u_f &= \sum_t G_t(\Omega_v) \cdot u_{f,t} \end{aligned}$$

The angular distribution of scattering is: 34

$$W_M(\lambda, \Omega_v, T) = W_M(\lambda, T) \cdot \frac{TG(\Omega_v) \cdot \Delta\Omega_v}{\sum_{v=1}^{N_{\text{dir}}} TG(\Omega_v) \cdot \Delta\Omega_v}$$

with 36

$$\begin{aligned} TG(\Omega_v) &= \sum_{i=1}^{N_{\text{dir}}} T_{\text{diff}}(\Omega_i, \Omega_v) \cdot G(\Omega_i) \cdot \Delta\Omega_i, T_{\text{diff}}(\Omega_i, \Omega_v) \\ &= \int_{\Delta\Omega_v} \frac{\int_{2\pi} \frac{g_f(\Omega_f)}{2\pi} \cdot |\Omega_i \cdot \Omega_f| \cdot f_d(\Omega_f, \Omega_s \rightarrow \Omega_v) \cdot d\Omega_f}{G(\Omega_s)} \\ &\quad \cdot d\Omega_v \end{aligned}$$

With \mathcal{T} leaf species: 38

$$\begin{aligned} TG(\Omega_v) &= \frac{\sum_t TG_t(\Omega_v) \cdot u_{f,t}}{\sum_t u_{f,t}} \Rightarrow W_M(\lambda, \Omega_v, T) \\ &= W_M(\lambda, T) \\ &\quad \cdot \frac{\sum_t TG_t(\Omega_v) \cdot u_{f,t} \cdot \Delta\Omega_v}{\sum_{v=1}^{N_{\text{dir}}} \sum_t TG_t(\Omega_v) \cdot u_{f,t} \cdot \Delta\Omega_v} \end{aligned}$$

The number of faces seen along Ω_v is $K \leq 3$: 40

$$W_M(\lambda, \Omega_v, T) = \sum_{k=1}^K W_{M \text{ face } k}(\lambda, \Omega_v, T, k)$$

1 with $W_{M \text{ face } k} \approx$ proportional to leaf area cross
2 section:

$$S_{\text{eff}}(u_f, \text{LAD}, \Omega_v, k) = \frac{W_{1 \text{ face } k}(\lambda, \Omega_v, T)}{L_B(\lambda, \Omega_v, T)}$$

4 Thus:

$$W_{M \text{ face } k}(\lambda, \Omega_v, T) = \frac{W_{1 \text{ face } k}(\lambda, \Omega_v, T)}{\sum_{v=1}^K W_{1 \text{ face } k}(\lambda, \Omega_v, T)} \cdot W_M(\lambda, \Omega_v, T)$$

6 Total energy that exits face k along (Ω_v) :

$$\begin{aligned} W_{\text{face } k}(\lambda, \Omega_v, T) &= W_{1 \text{ face } k}(\lambda, \Omega_v, T) \\ &\quad + W_{M \text{ face } k}(\lambda, \Omega_v, T) \\ &\Rightarrow W_{\text{face } k}(\lambda, \Omega_v, T) \\ &= L_B(\lambda, T) \cdot H_f(u_f, \text{LAD}, \Omega_v, k) \end{aligned}$$

8 where LAD

$$\begin{aligned} H_f(u_f, \text{LAD}, \Omega_v, k) &= S_{\text{eff}}(u_f, \text{LAD}, \Omega_v, k) \cdot \Delta\Omega_v \\ &\cdot \left[1 + \frac{S_{\text{eff}}(u_f, \text{LAD}, \Omega_v, k)}{\sum_{v=1}^K S_{\text{eff}}(u_f, \text{LAD}, \Omega_v, k)} \right. \\ &\cdot \frac{TG(\Omega_v) \cdot \Delta\Omega_v}{\sum_{v=1}^{N_{\text{dif}}} TG(\Omega_v) \cdot \Delta\Omega_{rv}} \cdot \frac{\omega_\lambda \cdot \langle T \rangle}{1 - \omega_\lambda \cdot [1 - \langle T \rangle]} \\ &\left. \cdot G(\Omega_v) \cdot u_f \cdot \int_{V_{\text{cell}}} (1 - e^{-G(\Omega_v) \cdot u_f \cdot \Delta l(dv)}) \cdot dv \right] \end{aligned}$$

In order to limit computer time, $H_f(u_f, \text{LAD}, \Omega_v, k)$ is pre-computed for:

- all exact $H_f(u_f, \text{LAD}, \Omega_v, k)$ values, if for each leaf species the number of u_f values is ≤ 10 .
- 10 $H_f(u_f, \text{LAD}, \Omega_v, k)$ values, if there is at least one leaf species for which the number of u_f values is > 10 . Pre-computation is performed on 10 equidistant u_f values from $u_{f, \text{min}}$ in to $u_{f, \text{max}}$ for each leaf species. In a 2nd step, the exact $H_f(u_f, \text{LAD}, \Omega_v, k)$ values are computed with a linear interpolation on the u_f values.

The precision of $W(\lambda, \Omega_v, T, k)$ depends on the H_f precision and thus on the discretization level of the sub-faces S_{ij} used to calculate leaf cell emission W_1 and scattering W_M . The estimate of $W(\lambda, \Omega_v, T, k)$ is all the more precise as this discretization is fine; i.e., large number $I \times J$ of sub-faces S_{ij} . Tests conducted with variable values of I and J showed that the pre-defined number $I \times J$ (50×50) lead to errors systematically lower than 0.01 K.

Figure 7 shows DART simulated directional brightness temperature $T_B(\Omega_v)$, as a function of view zenith angle θ_v , for a vegetation turbid medium (LAI=5), with 298 K leaf and soil temperature. It illustrates the impact of (1) the number

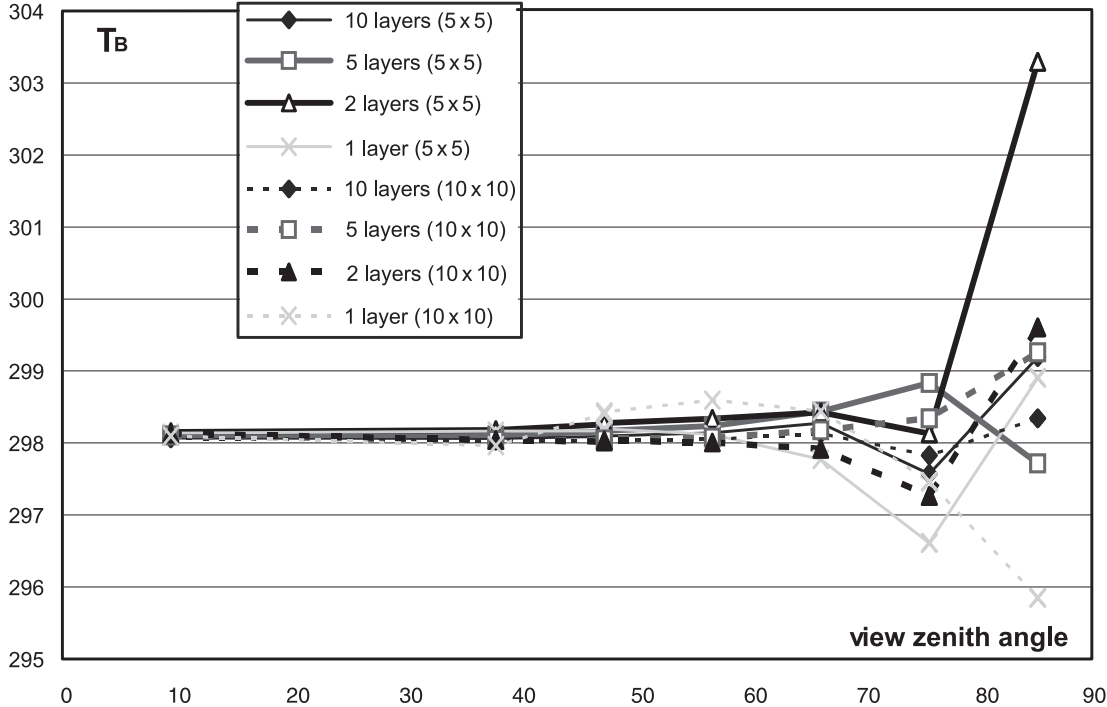


Fig. 7. Precision of $T_{\text{app}}(\Omega_v)$ according to the view zenith angle, the discretization N_{sf} (5×5 or 10×10) and the numbers of layers (1–10). LAI=5. $T_f = 298$ K

1 of $I \times J$ (5×5 and 10×10) sub faces used for
 2 computing the emission per cell face, and (2) the
 3 number of layers (1, 2, 5 and 10) used to simulate
 4 the turbid layer. Brightness temperature should
 5 be 298 K for any direction. As expected, errors
 6 decrease with the increase of the $I \times J$ value and
 7 the number of layers.

8 • Account of neighbor cells

9 Usually, the origin of any emitted ray $W_{\text{face } k}$
 10 should not be the center of a cell face. Indeed,
 11 the spatial distribution of energy $W_{\text{face } k}(\Omega_v, i, j)$
 12 is not uniform on the exit face k . Moreover,
 13 rays $W_{\text{face } k}(\Omega_v, i, j)$ that exit face k have differ-
 14 ent path lengths in the neighbor cells of the
 15 emitting cell, which implies that the transmis-
 16 sion of energy $W_{\text{face } k}(\Omega_v, i, j)$, starting from the
 17 center of the face k , through several neighbor
 18 turbid cells, differs from the sum of energies
 19 $W_{\text{face } k}(\Omega_v, i, j)$ transmitted, after exiting face k .
 20 Thus, for an upward direction in the Oyz
 21 plan (Fig. 6), with cells close to the transmit-
 22 ting cell characterized by a coefficient of pro-
 23 jection $G(\Omega_v)$ and a leaf volume density foliar
 24 $u_{f''}$, one has:

$$W_{\text{face } k}(\Omega_v) \cdot \exp[-G(\Omega_v) \cdot u_{f''} \cdot \Delta l_{\text{centre}}] \\ \neq < \sum_{i,j} W_{\text{face } k}(\Omega_v, i, j) \cdot \exp[-G(\Omega_v) \cdot u_{f''} \cdot \Delta l_{i,j}]$$

26 $\Delta l_{i,j}$ = distance from surface dS_{ij} to the hori-
 27 zontal plane of the top face of the emitting
 28 cell.

Tracking all individual rays requires much 29
 computer resource. Thus, we developed a solu- 30
 tion that is both accurate and efficient in terms 31
 of computer time, for any type of turbid cell. It 32
 determines a point $P(X_P, Y_P, Z_P)$ such that the 33
 energy $W_{\text{face } k}(\Omega_v)$ transmitted from P through 34
 several neighbor turbid cells is equal to the sum 35
 of all individual energies $W_{\text{face } k}(\Omega_v, i, j)$ trans- 36
 mitted. For example, for the right vertical face 37
 A (Fig. 6), co-ordinates X_P and Z_P of P verify 38
 the two equations: 39

– coordinate X_P : 40

$$W_{\text{face } k} \times \exp(-G(\Omega_v) \times u_{f''} \times Lx_P) \\ = \iint_S (W(x, z, \Omega_v, u_f, \text{LAD}, T, \lambda) \\ \times \exp(-G(\Omega_v) \times u_{f''} \times Lx) \cdot dS)$$

– coordinate Z_P : 42

$$W_{\text{face } k} \times \exp(-G(\Omega_v) \times u_{f''} \times Lz_P) \\ = \iint_S (W(x, z, \Omega_v, u_f, \text{LAD}, T, \lambda) \\ \times \exp(-G(\Omega_v) \times u_{f''} \times Lz) \cdot dS)$$

Lz_P : distance along (Ω_v) between a point P of 44
 face K and the horizontal plane that con- 45
 tains the upper or lower face of the emit- 46
 ting cell, depending if (Ω_v) is upward or 47
 downward. 48

Lx_P : distance along (Ω_v) between a point P of 49
 face K and the vertical plane that contains 50

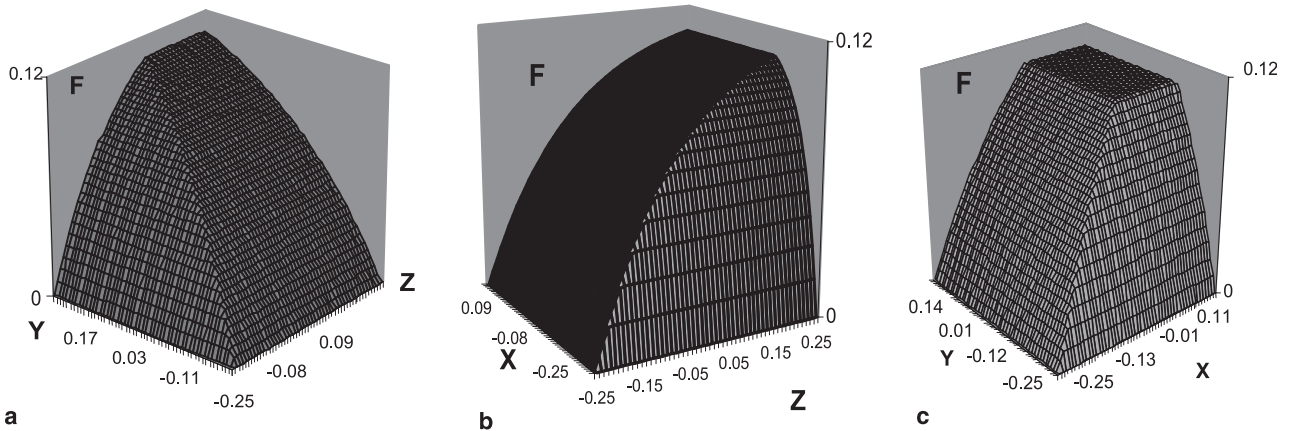


Fig. 8. 3-D relative distributions of the energy emitted by the faces of a turbid cell. (a) Front face ($x = \Delta X$): $F(y, z, \text{LAI}, \text{LAD})$. (b) Right face ($y = \Delta Y$): $F(x, z, \text{LAI}, \text{LAD})$. (c) Top face ($z = \Delta Z$): $F(x, y, \text{LAI}, \text{LAD})$. $\text{LAI} = 5$. $\Delta Y = \Delta Z = 0.5$. LAD spherical. $(\theta_v, \theta_v) = (60, 72)$

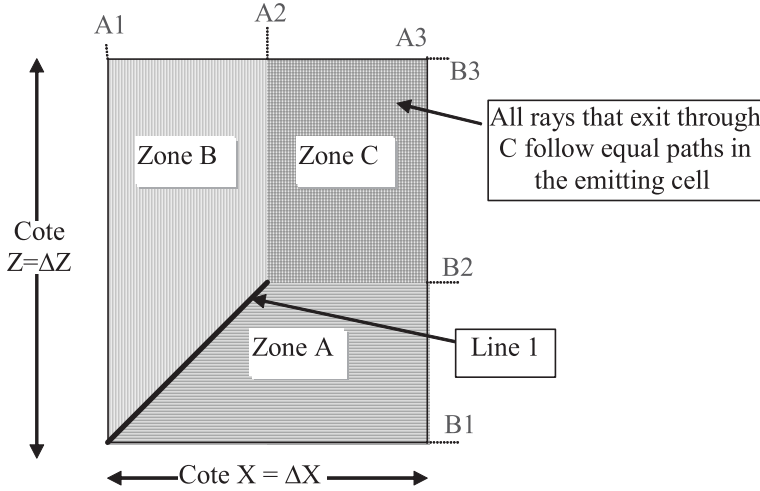


Fig. 9. 3-D schematic representation of distribution F

1 the front or back face of the cell, depending
 2 if (Ω_v) goes forward or backward.
 3 u_f : leaf volume density of the first cell crossed
 4 by the ray from P along (Ω_v) . It can be
 5 null.

6 The energy emitted by a cell along (Ω_v)
 7 through face k is proportional to " $L_B(\lambda, T) \times$
 8 cross section dS_{eff} of face k along (Ω_v) ". Position
 9 of P on face k depends on the relative directional
 10 distribution F of the energy emitted by the cell.
 11 For the cell face in the plane $\{y = \Delta Y\} > 0$, this
 12 distribution is:

$$F(x, z, \theta_v, \varphi_v, u_f, \text{LAD}) = \frac{W(x, z, \theta_v, \varphi_v, u_f, \text{LAD}, T, \lambda)}{L_B(\lambda, T) \times dS_{\text{eff}}}$$

14 Figure 8 shows the relative distribution F
 15 of the emitted energy through the front, right
 16 and top faces of an emitting turbid cell
 17 ($\text{LAI} = 5$, $\Delta Y = \Delta Z = 0.5$, spherical LAD),
 18 for direction $(\theta_v, \varphi_v) = (60, 72)$. Face center
 19 $(x, y, z \in [-0.25, 0.25])$ is the origin of co-ordinates.
 20 F appears to be the juxtaposition of 3
 21 zones (A, B, C) with generic shapes (Fig. 9)
 22 the limits of which are exponential curves. F
 23 is constant in zone C and has an exponential
 24 surface in zones A and B. These surfaces tend
 25 to be plane surfaces if LAI becomes small.
 26 They are characterized by 6 parameters (A1,
 27 A2, A3, B1, B2, B3) that depend on $(u_f,$
 28 LAD, $\Omega_v, k)$ values. These remarks suggest re-
 29 placing the integral expressions of F by analyti-
 30 cal expressions.

The case 'face $y = \Delta Y$ ' is analyzed. $F(x, z,$ 31
 LAI, LAD expressions differ in zones A, B and C: 32

– $M(x, z)$ in zone A ($z < B2$ and $z < a \cdot (x +$ 33
 $\frac{\Delta X}{2}) - \frac{\Delta Z}{2}$): 34

$F_A(x, z, \text{LAI}, \text{LAD})$

$$\omega \cdot \frac{[1 - \exp\left\{-\text{sign } e2 \cdot \text{LAI} \cdot \frac{(z - B1)}{|a|}\right\}]}{1 - \exp\left\{-\text{sign } e2 \cdot \text{LAI} \cdot \frac{(B3 - B1)}{|a|}\right\}}$$

– $M(x, z)$ in zone B ($x < A2$ and $z < a \cdot (x +$ 36
 $\frac{\Delta X}{2}) - \frac{\Delta Z}{2}$): 37

$F_B(x, z, \text{LAI}, \text{LAD})$

$$\omega \cdot \frac{[1 - \exp\{-\text{sign } e1 \cdot \text{LAI} \cdot (x - A1)\}]}{1 - \exp\{-\text{sign } e1 \cdot \text{LAI} \cdot (A3 - A1)\}}$$

– $M(x, z)$ in zone C ($x \in [A2, A3]$ and $z \in$ 39
 $[B2, B3]$): $F_C(x, z, \text{LAI}, \text{LAD}) = \omega$ 40

$\text{sign } e1 = \text{sign}(A3 - A1)$

$\text{sign } e2 = \text{sign}(B3 - B1)$

$$a = \frac{B2 - B1}{A2 - A1} \quad u_f = \frac{\text{LAI}}{\Delta Z}$$

$$\omega = \Delta\Omega_v \cdot (1 - \exp(-G \cdot u_f \cdot L))$$

$d\Omega_v$: solid angle of direction Ω_v . 42

L : longer path length of a ray within a cell. 43

a : parameter that allows to ensure the continu- 44
 ity of curves F_A and F_B 45

Function F is not appropriate if the direction 46
 of emission Ω_v is parallel with a face (e.g., 47

1 $\varphi = 90^\circ$). Then, the emission along Ω_v comes
 2 only from 1 or 2 faces (e.g., $\theta = 0$, $\varphi = 0$).

3 Calculation of the 3 co-ordinates of a point ori-
 4 gin P on a cell face, requires to integrate F and to
 5 verify some equations. For example, for the right
 6 face of the cell ($y = \Delta Y$), we must have:

$$W_{\text{face}} \times \exp(-G \cdot u_{f''} \cdot Lx_P) \\ = \iint_{\text{face}} (F_A + F_B + F_C) \cdot L_B(\lambda, T) \\ \cdot \exp(-G \cdot u_{f''} \cdot Lx) dS_{\text{eff}}$$

$$W_{\text{face}} \times \exp(-G \cdot u_{f''} \cdot Lx_P) \\ = \iint_{\text{face}} (F_A + F_B + F_C) \cdot L_B(\lambda, T) \\ \cdot \exp(-G \cdot u_{f''} \cdot Lz) dS_{\text{eff}}$$

9 Using:

$$Lx = \frac{(-\text{sign } e(\sin \theta \cdot \cos \varphi)) \cdot \text{Cote } X/2 - x}{\sin \theta \cdot \cos \varphi} \\ = \frac{\varepsilon_1 \cdot \text{Cote } X/2 - x}{\sin \theta \cdot \cos \varphi} \quad \text{with}$$

$$\varepsilon_1 = -\text{sign}(\sin \theta \cdot \cos \varphi)$$

$$Lz = \frac{(\text{sign } e(\cos \theta)) \cdot \text{Cote } X/2 - x}{\cos \theta} \\ = \frac{\varepsilon_3 \cdot \text{Cote } X/2 - x}{\cos \theta} \quad \text{with } \varepsilon_3 = \text{sign}(\cos \theta)$$

$$Ly = \frac{(-\text{sign } e(\sin \varphi \cdot \sin \theta)) \cdot \text{Cote } Y/2 - y}{\sin \varphi \cdot \cos \theta} \\ = \frac{\varepsilon_2 \cdot \text{Cote } Y/2 - y}{\sin \varphi \cdot \sin \theta} \quad \text{with}$$

$$\varepsilon_1 = -\text{sign}(\sin \theta \cdot \cos \varphi)$$

12 co-ordinates of P on the right face of the cell,

13 relative to the center of this cell, are:

$$x_P = \varepsilon_1 \cdot \text{Cote } X/2 + \frac{\cos \varphi \cdot \sin \theta}{G \cdot u_{f''}} \\ \cdot \ln \left(\frac{\iint_{\text{Zone A}} F_A \cdot L \cdot \exp(-G \cdot u_{f''} \cdot Lx) dS_{\text{eff}} + \iint_{\text{Zone B}} F_B \cdot L \cdot \exp(-G \cdot u_{f''} \cdot Lx) dS_{\text{eff}} + \iint_{\text{Zone C}} F_C \cdot L \cdot \exp(-G \cdot u_{f''} \cdot Lx) dS_{\text{eff}}}{W_{\text{face}}} \right)$$

$$z_P = \varepsilon_3 \cdot \text{Cote } Z/2 + \frac{\cos \theta}{G \cdot u_{f''}} \\ \cdot \ln \left(\frac{\iint_{\text{Zone A}} F_A \cdot L \cdot \exp(-G \cdot u_{f''} \cdot Lz) dS_{\text{eff}} + \iint_{\text{Zone B}} F_B \cdot L \cdot \exp(-G \cdot u_{f''} \cdot Lz) dS_{\text{eff}} + \iint_{\text{Zone C}} F_C \cdot L \cdot \exp(-G \cdot u_{f''} \cdot Lz) dS_{\text{eff}}}{W_{\text{face}}} \right)$$

Expressions of x_P , y_P and z_P are very interesting 14
 because they are analytical, which makes it pos- 15
 sible to calculate them with small computation 16
 times, for any configuration. 17

If there are \mathcal{T} leaf species, for each direction 18
 (Ω_v) and each cell face, the point P is the center 19
 of gravity of all \mathcal{T} points, weighted by the leaf 20
 volume densities $u_{f,t}$. 21

5.2 Opaque surfaces 22

For an opaque surface of direct-hemispheric re- 23
 flectance $\rho_{\text{dh}}(\lambda, T, \Omega_v) : \alpha_a(\lambda, T, \Omega_v) = 1 - \rho_{\text{dh}}(\lambda, 24$
 $T, \Omega_v)$. Moreover, $\rho_{\text{dh}}(\lambda, T, \Omega_v) = \rho_{\text{hd}}(\lambda, T, \Omega_v)$. 25
 Thus, with thermodynamic balance, in the ab- 26
 sence of mechanisms of energy exchange other 27
 than radiative (Hapke 1993), the emissivity is: 28

$$\varepsilon_d(\lambda, T, \Omega_v) = \alpha_a(\lambda, T, \Omega_v) = 1 - \rho_{\text{hd}}(\lambda, T, \Omega_v)$$

- Lambertian ρ_{lamb} + specular $\rho_{\text{spe,dh}}(\Omega) : \varepsilon_d(\lambda, T, 30$
 $\Omega_v) = 1 - \rho_{\text{lamb}} - \rho_{\text{spe,dh}}(\Omega_v)$ 31

- Hapke $\langle \rho \rangle$ + specular $\rho_{\text{spe,dh}}(\Omega) : \varepsilon_d(\lambda, T, \Omega_v) = 32$
 $1 - \langle \rho \rangle - \rho_{\text{spe,dh}}(\Omega_v)$ 33

We consider only the outwards emission, and 34
 not the inwards emission, by scene elements 35
 made of opaque figures. Thus, the internal emis- 36
 sion of houses is not introduced. This choice is 37
 explained by the fact that DART is mostly dedi- 38
 cated to the simulation of radiative transfer for 39
 remote sensing purpose and for the radiative bud- 40
 get of external surfaces of canopies. 41

Thus, a surface $(S, \Omega_n, \varepsilon_d)$ emits only in the 42
 hemisphere that contains its normal (Ω_n) : 43

$$W_e(\lambda, T, \theta_v) \cong \varepsilon_d \cdot L_B(\lambda, T) \times S \times \cos \psi_{nv} \\ \times \Delta \Omega_v \quad \text{if } \psi_{nv} \leq 90$$

$$W_e(\lambda, T, \theta_v) \cong 0 \quad \text{if } \psi_{nv} \geq 90$$

$$\cos \psi_{nv} = \cos \theta_n \cdot \cos \theta_v + \sin \theta_n \\ \cdot \sin \theta_v \cdot \cos(\psi_{nv})$$

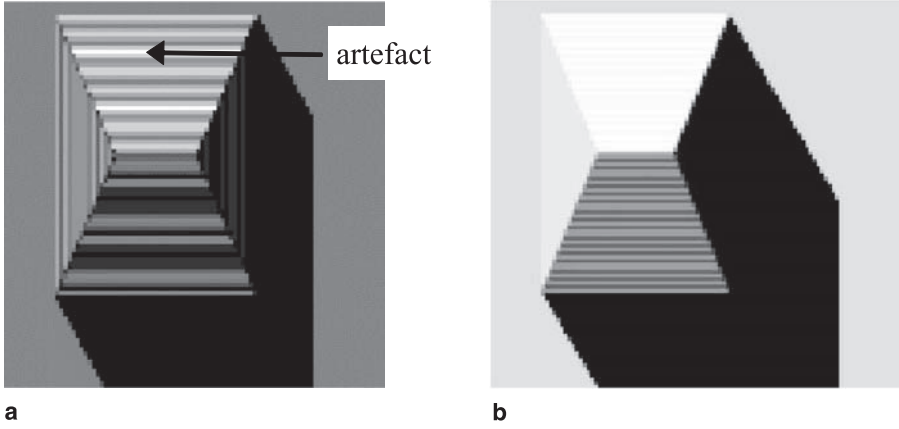


Fig. 10. Computation of T_{figure} , without (a) and with (b) account of the area of figures

1 Once emitted by a cell, a ray $W(\Omega_v)$ is tracked in
2 the 3D scene, where it can be:

- 3 • completely intercepted by an opaque surface,
4 to be scattered in the following iteration, or.
- 5 • partly intercepted by turbid cells or not inter-
6 cepted at all. Part of $W(\Omega_v)$ that reaches a
7 cell $(\Delta X, \Delta Y)$ of scene top layer, increases the
8 energy $W_{\text{c-fict}}(\Omega_v)$ already stored by this cell.

9 After the last iteration, $W_{\text{c-fict}}(\Omega_v)$ is translated
10 into scene brightness temperature $T_B(\Omega_v)$.

$$T_B(\theta_v) = \frac{h \cdot C / \lambda \cdot k}{\ln \left(\frac{2 \cdot h \cdot C^2}{\lambda_o^5 \cdot (W_{\text{c,lop}}(\Omega_v) / \cos(\theta_v) \times \Delta\Omega_v \times \Delta X \times \Delta Y) + 1} \right)}$$

11 In the case of a simulation with $\Delta\lambda \approx 0$, λ_o is
12 the mean wavelength. This choice is not possible
13 if $\Delta\lambda \neq 0$. In that case, the inversion is con-
14 ducted with a reference wavelength that depends
15 on the scene mean temperature T_{mean} (Dallhuin
16 2002). λ_o verifies:

$$L_B(\lambda_o, T_{\text{mean}}) = \frac{1}{\Delta\lambda} \cdot \int_{\lambda_{\min}}^{\lambda_{\max}} L(\lambda, T_{\text{mean}}) \cdot d\lambda \\ \neq L \left(\frac{\lambda_{\min} + \lambda_{\max}}{2}, T_{\text{mean}} \right)$$

18 Two approaches can be used to specify the 3D
19 temperature of the scene:

- 20 – 3D matrix of cell temperature values. This ma-
21 trix can be computed by the DARTEB model
22 (see last chapter). In that case, TIR emission
23 of any opaque figure is simulated from the
24 “geometric” barycentre of that figure.

- scene illumination in the visible spectral do-
25 main. The temperature of any scene element is
26 proportional to visible scene irradiance and is
27 within a pre-defined interval that is specific for
28 each type of scene element: soil, wall, roof,
29 etc. The limited number of rays that simulate
30 scene illumination necessarily introduces arti-
31 facts. These are reduced (1) using a larger
32 number of illuminating rays per cell of the
33 scene upper layer (pre defined number is 49),
34 (2) by accounting the area of each emitting
35

opaque figure (Fig. 10) for calculating its tem-
36 perature T_{figure} , and (3) by equalizing the tem-
37 perature of all coplanar figures in the same
38 cell. TIR emission of opaque figures is simu-
39 lated from the “energy” barycentre for illu-
40 minated figures, and from the “geometric”
41 barycentre for “non illuminated figures”.
42

6. Application to CAPITOU project

43

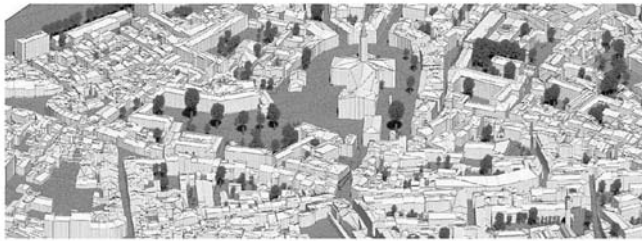
The new DART model was used in the context of
44 the CAPITOU experiment that took place over
45 the city of Toulouse, France, from February 2004
46 to February 2005. Study of urban energy balance
47 was one of the objectives. For that, different
48 types of measurements took place: acquisition
49 of TIR airborne images, in-situ measurements
50 of turbulent fluxes, surface energy balance, sur-
51 face temperatures, etc. (Masson et al. 2007).
52

1 DART was used for simulating both remote
 2 sensing images in visible, NIR and TIR spectral
 3 bands and the 3D radiative budget. Moreover, the
 4 DARTEB model used this simulated radiative
 5 budget for assessing the time evolution of surface
 6 variables such as wall temperatures and heat sen-
 7 sible fluxes. DARTEB is a model that is being
 8 developed for calculating the 3D (3 dimensional)
 9 energy budget of urban and natural scenes,

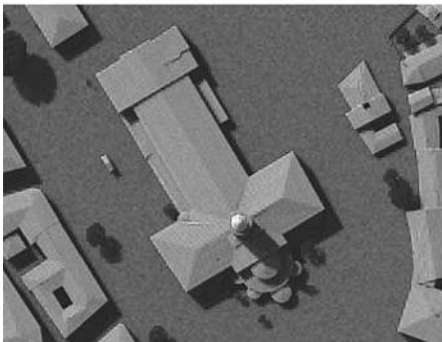
possibly with topography and atmosphere. It ac- 10
 counts for all energy mechanisms (heat conduc- 11
 tion, turbulent momentum and heat fluxes, water 12
 reservoir evolution, vegetation photosynthesis, 13
 evapotranspiration) that contribute to the energy 14
 budget. In the case of a urban canopy, it simulates 15
 non radiative mechanisms with the equations of 16
 the TEB urban surface scheme (Masson 2000). 17
 This scheme works with a canyon geometry. 18



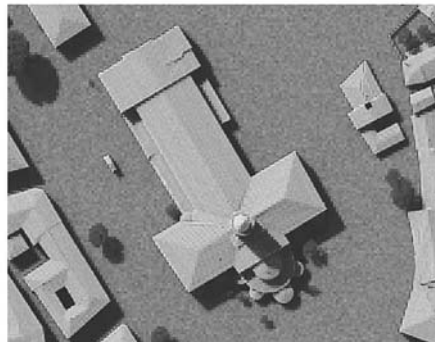
a



b



c



d

Fig. 11. DART simulated nadir (a) and oblique (b) images of St Sernin district. (c) and (d) show the St Sernin basilica (centre (a)) for a sensor below and on top of the atmosphere. Red spectral band

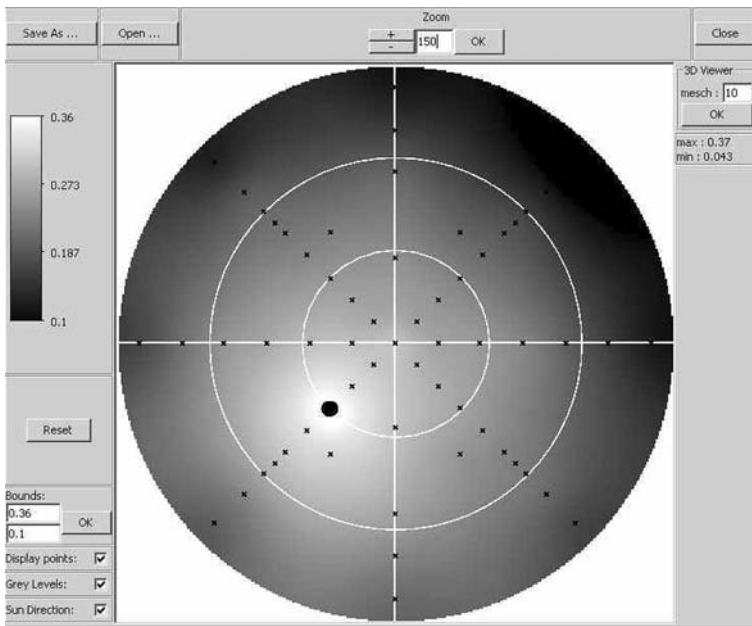


Fig. 12. Example of near infrared BRF of St Sernin district. It is computed by the DART graphic user interface with simulated reflectance values (crosses), for a sun direction shown by a black circle. Distance from the circle centre gives the view zenith angle ($[0\ 90^\circ]$) and the anti clockwise angle from the horizontal axis gives the azimuth view angle ($[0\ 360^\circ]$)

1 6.1 DART simulated remote sensing images

2 First, a program was developed for importing the
 3 urban database (Autocad format) of the Toulouse
 4 town hall as a DART scene. This led to the crea-
 5 tion of DART objects (e.g., houses and trees).
 6 The fact that urban elements in the data base
 7 are not houses or buildings but unrelated individ-
 8 ual walls and roofs was a difficulty. The local
 9 digital elevation model (DEM) was also import-
 10 ed. Figure 11 shows nadir (a) and oblique (b)
 11 color composites of the St Sernin district of
 12 Toulouse city. They were created with DART
 13 simulations in the blue, green and red spectral
 14 bands. Simulations stress that urban reflectance
 15 and brightness temperature values display a
 16 marked angular heterogeneity. This heterogene-
 17 ity is illustrated here with the angular distribu-
 18 tion of NIR reflectance values of St Sernin district
 19 (Fig. 12).

20 Figure 11c and d display DART remote sens-
 21 ing images of St Sernin basilica, in the center of
 22 St Sernin district. They are simulated for a sensor
 23 at the bottom of the atmosphere (i.e., BOA im-
 24 age) and for a sensor at the top the atmosphere
 25 (TOA). The bluish tone of the TOA image, com-
 26 pared to the BOA image, is due to the fact that
 27 atmosphere scatters more in the blue than in
 28 the red spectral domain. The realistic aspect of
 29 DART images is encouraging. However, the ob-
 30 jective of DART is to simulate satellite images

with accurate geometric and radiometric charac- 31
 32 teristics. This is necessary for studying Earth sur- 33
 34 faces from space, using a physical approach such 35
 36 as image inversion (Gastellu-Etchegorry et al. 37
 38 2003). Although DART was already validated for 38
 39 the visible and NIR spectral domains (Widlowski 39
 40 et al. 2007) and partly validated for the TIR do- 40
 main (Guillevic et al. 2003), in the future, it should 40
 be also validated for TIR radiative transfer in ur- 40
 ban canopies with satellite images.

6.2 DARTEB energy budget simulation 41

42 DARTEB simulates the energy budget of urban 42
 43 and vegetation canopies. For that, it uses the 3-D 43
 44 DART radiative budget and it models all physical 44
 45 phenomena, other than radiation, that contribute 45
 46 to the energy budget. In the case of urban cano- 46
 47 pies, turbulent fluxes and conduction are compu- 47
 48 ted with classical boundary-layer laws using 48
 49 equations of the TEB model (Masson 2000). 49
 50 However, conversely to TEB model DARTEB 50
 51 uses a 3-D cell discretization, in addition to the 51
 52 layer discretization of roofs, walls and roads: 52
 53 modeling is conducted on a DART cell per cell 53
 54 basis. As a result, fluxes are computed for each 54
 55 point of the 3-D scene. The transfer coefficients 55
 56 for turbulent heat and moisture fluxes are identi- 56
 57 cal; they differ from the transfer coefficients for 57
 58 momentum fluxes. For DARTEB, the urban can- 58

1 opy is simulated as the juxtaposition of urban
 2 street canyons. Here, we worked with a single
 3 urban canyon (Fig. 13), for remaining in the va-

4 lidity domain of TEB equations (Masson 2000).
 5 Most major variables used by DARTEB are men-
 6 tioned in Fig. 13. Each surface type (wall, soil,

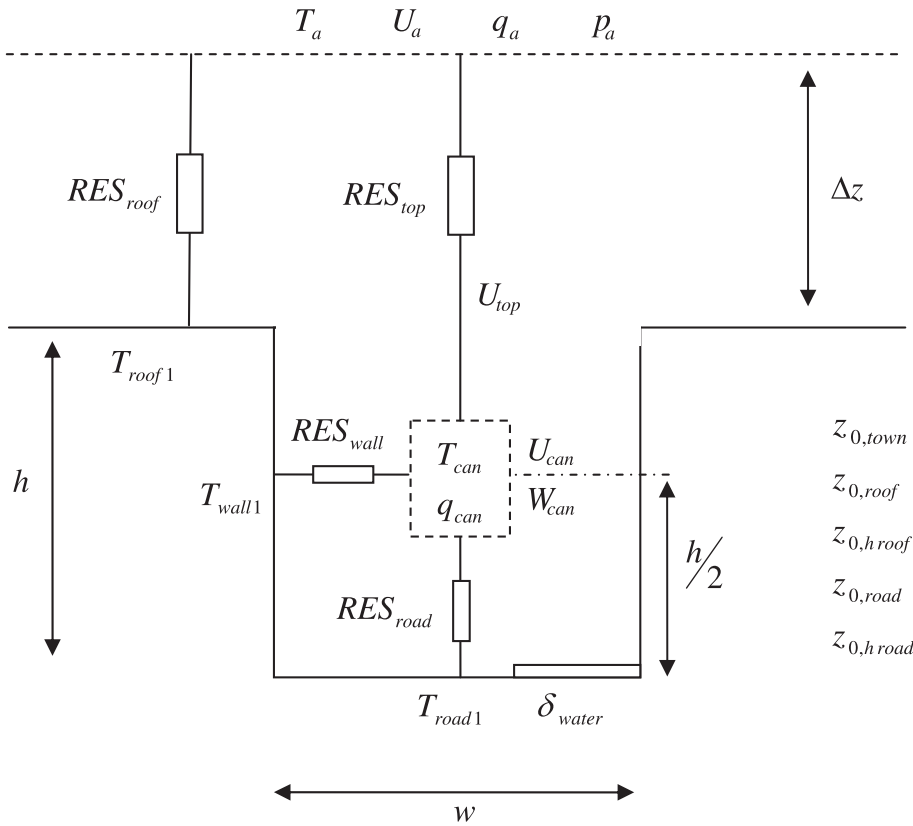


Fig. 13. Simulation of the canyon. Parameters used by DARTEB are listed below. U_a, T_a, q_a, p_a : Wind speed and air temperature/humidity/pressure at 1st atmosphere layer. h, w : Canyon height and width. Δ_z : Height of measurements above the roof, U_{top} : wind speed right above the canyon. $T_{roof1}, T_{wall1}, T_{road1}$: Roof, wall and road temperatures. RES_{top}/RES_{roof} : Aerodynamic resistance between the atmosphere and the canyon/roof, RES_{wall}/RES_{road} : Aerodynamic resistance between the canyon and the wall/road, $U_{can}/W_{can}, T_{can}, q_{can}$: Canyon horizontal/vertical wind speed and air temperature/humidity, $z_{0,roof}, z_{0,h roof}, z_{0,road}, z_{0,h road}$: Roof and road dynamic and thermal roughness lengths. $z_{0,town}$: Town dynamic roughness length. δ_{eau} : Percentage of wet road

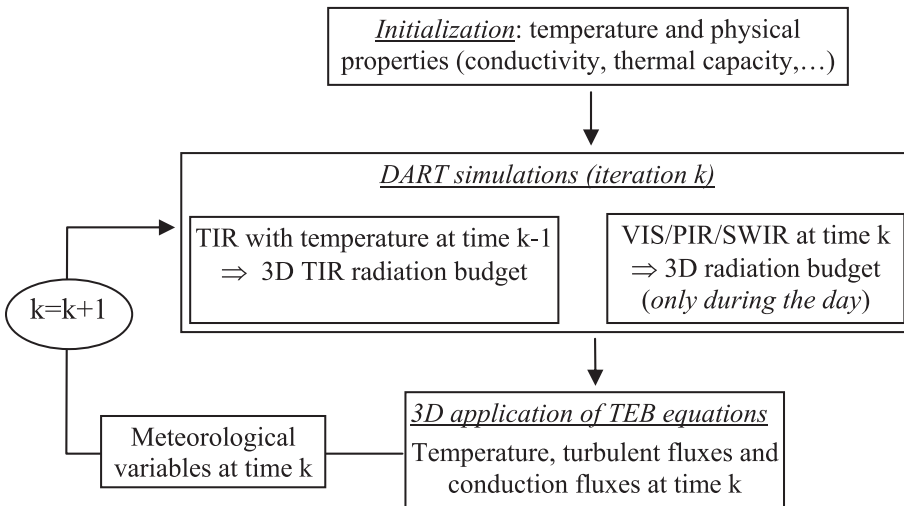


Fig. 14. Diagram of DARTEB model

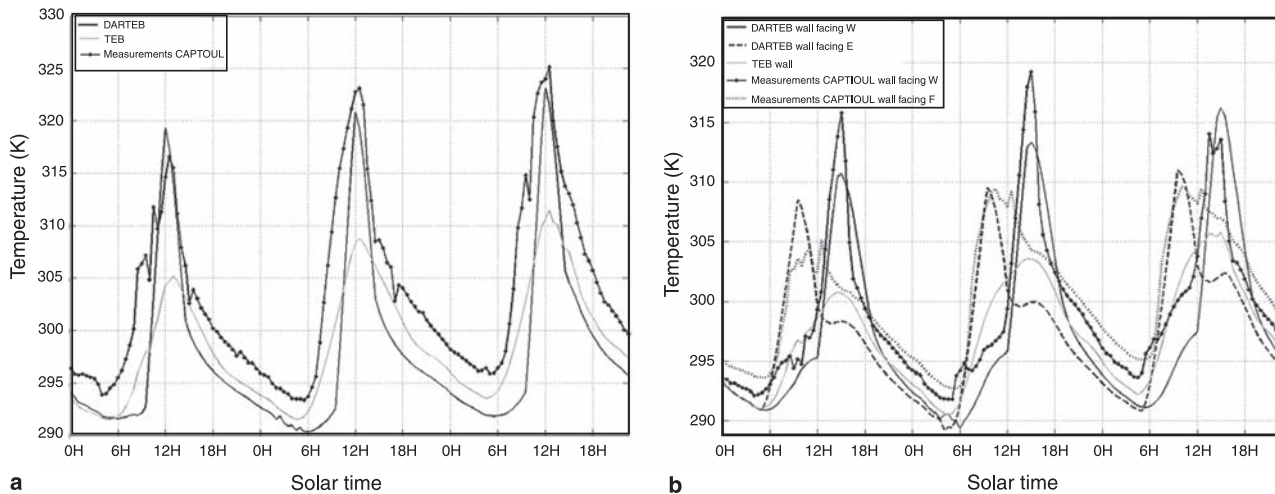


Fig. 15. Comparison of temperature measurements with DARTEB and TEB simulations. July 14–16 2004. (a) Road of La Pomme street (Toulouse) with a south East – North West orientation. (b) Walls of Alsace Lorraine street (Toulouse) with a South-North orientation. The 2 walls are facing West and East directions, which implies different thermal behaviors

1 roof) is discretized into several layers for simulating the conduction fluxes to or from the ground and building interiors. The number of layers for road, wall and roof can differ. A minimal number of three layers is advised because temperature gradients can be large and because of the multi-layer structure of the walls and roofs.

9 DARTEB uses a prognostic approach (Fig. 14) for assessing the 3D radiative budget distribution, and consequently the 3D temperature distribution. Temperature values at time “ $k-1$ ” are used for computing the 3D TIR and energy budgets at time “ k ”, which allows one to compute the 3D temperature distribution at time “ k ”, using the 3D visible and NIR radiation budget at time “ k ” (Fig. 14). DART simulations in the short wave domain are conducted during the day period only.

20 The validity of DARTEB was tested against TEB simulations and against in situ temperature measurements during the Capitoul campaign (Albinet 2008). DARTEB proved to be coherent with TEB and with measurements. Here, this is illustrated by the comparison of simulated and measured temperatures during 3 days, from July 27 14 to July 17, 2004, for the Alsace Lorraine street (South-North orientation) and La Pomme street (South East – North West orientation) in 29 Toulouse.

31 The simulated and measured road temperature curves are very similar (Fig. 15a). As expected, 32 road temperature values increase during the day. 33 There are 3 major differences between DARTEB and TEB simulations. (1) Maximal DARTEB 34 temperatures are larger than maximal TEB 35 temperatures. (2) Maximal DARTEB temperatures 36 occur before midday conversely to maximal 37 TEB temperatures that occur at midday. (3) 38 DARTEB curves are smoother than TEB curves. 39 These differences are mostly explained by the fact 40 that DARTEB takes into account the 3-D nature 41 of the canyon geometry, conversely to TEB. 42 43

44 Indeed, the TEB model works with a mean 45 canyon that corresponds to an azimuthally averaged 46 street direction. Thus, TEB temperatures 47 are mean values, which explains that their time 48 variations are smoothed, with maximal values 49 at midday. Actually, due to the South East – 50 North West orientation of La Pomme street, the 51 maximum road illumination occurs before mid- 52 day and the maximal road illumination is larger 53 than the mean road illumination for all possible 54 canyon orientations. This is well simulated by 55 DARTEB. Each morning, the measured and 56 DARTEB temperature values display nearly the 57 same sharp increase. However, each afternoon, 58 DARTEB temperature values decrease faster 59 than TEB and the observed temperature values. 60 Several factors can explain the differences be-

1 tween the DARTEB and observed temperature
 2 values. For example, an inaccurate road heat ca-
 3 pacity implies an inaccurate conduction flux, and
 4 an inaccurate road roughness length tends to im-
 5 ply an inaccurate heat flux, which tends to lead to
 6 inaccurate road temperature values. Another pos-
 7 sible explanation can come from an inaccurate
 8 simulation of the proportions of the 2 compo-
 9 nents of the canyon illumination: sun and sky
 10 illumination. Here, these components are driven
 11 by the atmosphere optical depth and sun zenith
 12 angle. However, in the absence of measurements,
 13 the atmosphere optical depth is assumed to be
 14 constant.

15 The wall (Fig. 15b) DARTEB and measured
 16 temperature values tend to be very close, both
 17 for the wall facing West, and for the wall facing
 18 East. They differ from TEB temperature values
 19 because TEB gives a mean value for the 2 walls
 20 of the canyon. Account of wall orientation is im-
 21 portant because walls with different sun illumi-
 22 nation have different temperature values, with
 23 larger values during daytime for walls with best
 24 sun orientation. As expected, DARTEB maximal
 25 temperature values occur in the morning for the
 26 wall facing East, and in the afternoon for the wall
 27 facing West. This is not the case with TEB maxi-
 28 mal temperature values; they occur at midday
 29 due to the fact that TEB works with azimuthally
 30 averaged canyons. This explains also that TEB
 31 temperature values are too small. These exam-
 32 ples stress the impact of 3-D architecture on tem-
 33 perature distributions.

34 7. Conclusion

35 Some major and recent improvements of DART
 36 radiative transfer model are presented in this pa-
 37 per. Thanks to these improvements, the DART
 38 model can simulate the radiation budget and re-
 39 mote sensing images of urban and natural land-
 40 scapes, with atmosphere and topography. Urban
 41 landscapes are simulated as the juxtaposition
 42 of opaque figures (i.e., triangles and parallelo-
 43 grams). A few basic urban elements are pre-de-
 44 fined for easing the building of urban landscapes:
 45 houses with different roofs, low walls, roads,
 46 etc. Opaque figures are characterized by spe-
 47 cific optical properties: lambertian, specular or
 48 Hapke reflectance/emissivity. In order to im-
 49 prove DART radiometric accuracy, the origin of

the path of any scattered and/or emitted ray is 50
 either a sub-cell center or a cell sub-face center. 51

In order to avoid repetitive calculations when 52
 simulating radiative transfer, which is costly in 53
 terms of computation time, some components of 54
 the emission by turbid cells and opaque figures 55
 are pre-computed. For example, the intensity that 56
 turbid cells emit is pre-computed for each turbid 57
 cell type (i.e., ρ_f , τ_f , LAD), for each cell face, for 58
 a range of volume density values u_f , and for 59
 each direction Ω_v . Moreover, emitted rays start 60
 from a point on cell faces, with a location that 61
 is analytically computed using pre-computed 62
 parameters that depend on the characteristics of 63
 the emitting cell and of cells that bound the emit- 64
 ting cell. 65

DART was used in the context of the Capitoul 66
 project (Masson et al. 2007). The objective was 67
 to test its potential for simulating remote sensing 68
 images and the radiation budget of urban cano- 69
 pies. For that, the Toulouse urban database was 70
 imported as a DART scene. Resulting simulated 71
 satellite images stressed the potential of DART 72
 for urban studies using remote sensing measure- 73
 ments. Moreover, DART simulated 3D radiation 74
 budget proved to be a valuable input for model- 75
 ing the 3D energy budget and heat fluxes with the 76
 DARTEB model. Results show that DARTEB 77
 simulated temperature values compare very well 78
 with in situ measurements, with results even bet- 79
 ter than TEB model. These better results are 80
 surely due to the fact that the DARTEB radiation 81
 budget is more accurate than the TEB radiation 82
 budget. Moreover, the DARTEB 3-D calculation 83
 of fluxes (i.e., on a cell per cell basis) affects 84
 also results. Work is being continued for better 85
 understanding differences between DARTEB 86
 and in situ measurements and TEB simulations 87
 on the other hand. An important objective is 88
 to determine in which case the account of 3D 89
 information, instead of 2D information as in 90
 the TEB scheme, is needed for accurate urban 91
 studies. 92

The DART code with the above mentioned 93
 improvements was recently professionalized by 94
 Magellium (www.magellium.fr) for Linux and 95
 Window systems, with the support of French 96
 Space Center (CNES). Work is still conducted 97
 for obtaining a reference model for remote sens- 98
 ing studies. DART is patented (PCT/FR 02/ 99
 01181). Paul Sabatier University (France) pro- 100

1 vides free licenses for scientific works (www.cesbio.ups-tlse.fr).

3 Annex

4 In DART model, there are 4 possible types of reflectance for
5 the opaque surfaces.

6 • *Type 0*: “Lambertian + random spatial variability”.

$$\rho(\Omega_s, \Omega_v) = \rho_{\text{lamb}} + \text{standard deviation } \sigma\rho.$$

8 • *Type 1*: “Lambertian + specular reflectance $\rho_{\text{spec}}(\Omega_s, \Omega_v)$ ”.

$$\rho(\Omega_s, \Omega_v) = \rho_{\text{lamb}} + \rho_{\text{spec}}(\Omega_s, \Omega_v)$$

10 DART discretization of directions complicates specular
11 reflectance modeling because there may be no discrete direc-

This allows one to define the direct-hemispheric reflectance factor:

$$\rho_{\text{spe,dh}}(\Omega_s) = \frac{W_{\text{spe}}(\Omega_s)}{W_{\text{int}}(\Omega_s)} = \pi \cdot \left\{ \left[\frac{\text{tg}(\theta_i - \theta_t)}{\text{tg}(\theta_i + \theta_t)} \right]^2 + \left[\frac{\sin(\theta_i - \theta_t)}{\sin(\theta_i + \theta_t)} \right]^2 \right\} \cdot A \cdot \frac{\alpha^4}{64} \cdot \left[1 - \frac{\alpha^2}{72} \right]$$

A surface S illuminated by an isotropic radiance L intercepts $W_{\text{int}}(\Omega_s) = \int L \cdot S \cdot \cos \theta_s \cdot d\Omega_s$. DART discrete directions have small solid angles $\Delta\Omega_i$. Thus:

$$\sum_i \cos \theta_i \cdot \Delta\Omega_i = 2\pi \cdot \sum_i \cos \theta_i \cdot \sin \theta_i \cdot \Delta\theta_i \approx \pi.$$

This allows one to define the hemispheric-hemispheric reflectance factor:

$$\rho_{\text{spe,hh}}(\Omega_s) = \frac{\int W_{\text{spe}}(\Omega_s) \cdot d\Omega_s}{\int W_{\text{int}}(\Omega_s) \cdot d\Omega_s} \approx \frac{\sum_i \pi \cdot \left\{ \left[\frac{\text{tg}(\theta_i - \theta_t)}{\text{tg}(\theta_i + \theta_t)} \right]^2 + \left[\frac{\sin(\theta_i - \theta_t)}{\sin(\theta_i + \theta_t)} \right]^2 \right\} \cdot A \cdot \frac{\alpha^4}{64} \cdot \left[1 - \frac{\alpha^2}{72} \right] L \cdot S \cdot \cos \theta_i \cdot \Delta\Omega_i}{\sum_i L \cdot S \cdot \cos \theta_i \cdot \Delta\Omega_i}$$

$$\Rightarrow \rho_{\text{spe,hh}}(\Omega_s) \approx \pi \cdot A \cdot \frac{\alpha^4}{32} \cdot \left[1 - \frac{\alpha^2}{72} \right] \cdot \sum_i \left\{ \left[\frac{\text{tg}(\theta_i - \theta_t)}{\text{tg}(\theta_i + \theta_t)} \right]^2 + \left[\frac{\sin(\theta_i - \theta_t)}{\sin(\theta_i + \theta_t)} \right]^2 \right\} \cdot \cos \theta_i \cdot \sin \theta_i \cdot \Delta\theta_i$$

12 tion that coincides with the Fresnel specular direction; *i.e.* a
13 direction that depends on the incident ray direction and on
14 the scatterer orientation.

15 Specular energy scattered is assumed to occur in a cone
16 of angular width α , with a value $W_{\text{spe}}(\Omega_v^*)$ along (Ω_v^*) that
17 decreases quadratically like “ $\left[\frac{\alpha^2}{4} - \Psi_{\text{vv}^*}^2 \right]$ ” from the Fresnel
18 specular direction. Its total value $W_{\text{spe}}(\Omega_s)$ is assumed to be
19 proportional to the intercepted incident radiation $W_{\text{int}}(\Omega_s)$, to
20 the theoretical Fresnel reflectance (*i.e.*, function of the refrac-
21 tion index $n(\lambda)$) and to a weight A.

$$W_{\text{spe}}(\Omega_s) = \int_0^{\alpha/2} \frac{1}{2} \cdot \left\{ \left[\frac{\text{tg}(\theta_i - \theta_t)}{\text{tg}(\theta_i + \theta_t)} \right]^2 + \left[\frac{\sin(\theta_i - \theta_t)}{\sin(\theta_i + \theta_t)} \right]^2 \right\} \cdot A \cdot \left[\frac{\alpha^2}{4} - \Psi_{\text{vv}^*}^2 \right] \cdot \sin \Psi_{\text{vv}^*} \cdot d\Psi_{\text{vv}^*} \cdot 2\pi \cdot W_{\text{int}}(\Omega_s)$$

23 where θ_i and θ_t are the zenith angles of the incident and
24 refracted rays, with $\sin \theta_t = n \cdot \sin \theta_i$

25 With $\alpha \ll 1$, we have $\sin \Psi_{\text{vv}^*} = \Psi_{\text{vv}^*} - \frac{1}{6} \cdot \Psi_{\text{vv}^*}^3$ for all
26 directions of the specular scattering cone. As a result:

$$W_{\text{spe}}(\Omega_s) = \pi \cdot W_{\text{int}}(\Omega_s) \cdot \left\{ \left[\frac{\text{tg}(\theta_i - \theta_t)}{\text{tg}(\theta_i + \theta_t)} \right]^2 + \left[\frac{\sin(\theta_i - \theta_t)}{\sin(\theta_i + \theta_t)} \right]^2 \right\} \cdot A \cdot \int_0^{\alpha/2} \left[\frac{\alpha^2}{4} - \Psi_{\text{vv}^*}^2 \right] \cdot \left[\Psi_{\text{vv}^*} \cdot \frac{1}{6} \Psi_{\text{vv}^*} \right] \cdot d\Psi_{\text{vv}^*}$$

$$W_{\text{spe}}(\Omega_s) = \pi \cdot W_{\text{int}}(\Omega_s) \cdot \left\{ \left[\frac{\text{tg}(\theta_i - \theta_t)}{\text{tg}(\theta_i + \theta_t)} \right]^2 + \left[\frac{\sin(\theta_i - \theta_t)}{\sin(\theta_i + \theta_t)} \right]^2 \right\} \cdot A \cdot \frac{\alpha^4}{64} \cdot \left[1 - \frac{\alpha^2}{72} \right]$$

Modeling multiple scattering by specular surfaces uses
 $\rho_{\text{spe,hh}}(\Omega_s)$. Indeed, for multiple scattering, specular surfaces
are assumed to be lambertian with a reflectance coefficient
equal to {lambertian reflectance ρ_{lamb} + average specular
reflectance $\rho_{\text{spe,hh}}$ }.

It results that $W_{\text{spe}}(\Omega_s)$ is equal to the theoretical
specular radiation (Fresnel) weighted by the factor
 $\pi \cdot A \cdot \frac{\alpha^4}{32} \cdot \left[1 - \frac{\alpha^2}{72} \right]$, usually less than 1. Being reflected
in a cone of half angle $\alpha/2$, it must be distributed in all
the \mathcal{D} angular sectors $(\Omega_v, \Delta\Omega_v)$ that intersect the specular
cone $\Delta\Omega_v = 2\pi \cdot (1 - \cos \frac{\alpha}{2})$. Source vectors $W_{\text{spe}}(\Omega_v,$
 $\Delta\Omega_v)$ are computed for any direction $(\Omega_v, \Delta\Omega_v)$ using
the approximations and the algorithm presented below.

– Approximations used for ensuring: $\sum_{\mathcal{D}} W_{\text{spe}}(\Omega_v, \Delta\Omega_v) = W_{\text{spe}}(\Omega_s)$. 50 51

$$W_{\text{spe}}(\Omega_v, \Delta\Omega_v) \approx W_{\text{spe}}(\Omega_s) \cdot \frac{\Delta\Omega_v \cdot \left[\frac{\alpha^2}{4} - \Psi_{\text{vv}^*}^2 \right]}{\sum \Delta\Omega_v \cdot \left[\frac{\alpha^2}{4} - \Psi_{\text{vv}^*}^2 \right]}$$

if $|\Psi_{\text{vv}^*}| < \frac{\alpha}{2}$ and $\Delta\Omega'_v = \Delta\Omega_v \cap \text{specular cone}$

$$W_{\text{spe}}(\Omega_v, \Delta\Omega_v) = 0 \quad \text{if } |\Psi_{\text{vv}^*}| > \frac{\alpha}{2}$$

– Approximations used for avoiding to compute the inter-
section of solid angles 55

$$\Delta\Omega'_v = \Delta\Omega_v \quad \text{if } \left\{ \Delta\Omega_v < \Delta\Omega_v^* \quad \text{and} \quad |\Psi_{\text{vv}^*}| < \frac{\alpha}{2} \right\}$$

$$\Delta\Omega'_v = \Delta\Omega_v^* \quad \text{if } \left\{ \Delta\Omega_v > \Delta\Omega_v^* \quad \text{and} \quad |\Psi_{\text{vv}^*}| < \frac{\alpha}{2} \right\}$$

and $\Delta\Omega'_v = 0$ if $|\Psi_{\text{vv}^*}| > \frac{\alpha}{2}$

1 – Algorithm:

- 2 a) Determination of the angles (θ_v^*, ϕ_v^*) of the specular
3 direction (Ω_v^*) :
4 Let β the angle between the surface normal Ω_n and the
incident direction Ω_i . For any Ω_i , $\beta = \theta_v^*$, the vectors
 Ω_i , Ω_v^* et Ω_n must be coplanar and the phase angle
must verify $(\Omega_i, \Omega_v^*) = 2 \cdot \beta$. With the notation “ $\theta_s =$
 $\pi - \theta_i$, $\phi_s = \phi_i$ ”, Ω_v^* is calculated from: $\Omega_v^* + \Omega_s =$
10 $2 \cos \beta \Omega_n$
11 b) Determination of the \mathcal{D} directions that verify
 $|\Psi_{vv^*}| < \frac{\alpha}{2}$.
12 c) Calculation of $\Delta \Omega_v' \cdot [\frac{\alpha^2}{4} - \Psi_{vv^*}^2]$ for every direction.
- 13 • *Type 2: “Hapke + specular”.*

$$\rho(\Omega_s, \Omega_v) = \rho_{\text{Hapke}}(\Omega_s, \Omega_v) + \rho_{\text{spec}}(\Omega_s, \Omega_v)$$

15 The component ρ_{Hapke} is calculated with a modeling
16 that assimilates an opaque figure to a plane medium made
17 of particles randomly distributed and large compared to
18 wavelength (Hapke 1993). The phase function $P(g_1, g_2)$
19 of particles, fitted by a Legendre polynomial, simulates
20 backscattering and forward scattering (Jacquemoud et al.
21 1992). Phase angle g_1 is defined as the angle between the
22 incident sun direction (Ω_s) and the view direction (Ω_v) . g_2
23 is defined as the angle between the specular direction (Ω_{v^*})
24 and (Ω_v) :

$$\rho_{\text{Hapke}}(\Omega_s, \Omega_v, \Omega_n) = \frac{\omega}{4} \cdot \frac{1}{\cos(\Psi_{in}) + |\cos(\Psi_{sn})|}$$

$$\cdot [[1 + B(g_1)] \cdot P(g_1, g_2)$$

$$+ H(\omega, |\cos(\Psi_{sn})|)$$

$$\cdot H(\omega, \cos(\Psi_{in}) - 1]$$

$$B(g_1) = \frac{B_0}{1 + \frac{1}{h} \cdot \tan\left(\frac{g_1}{2}\right)} \quad H(\omega, x) = \frac{1 + 2 \cdot x}{1 + 2 \cdot \gamma \cdot x}$$

$$\gamma = (1 - \omega)^{0.5}$$

$$P(g_1, g_2) = 1 + b_1 \cdot \cos g_1 + c_1 \cdot \frac{3 \cdot \cos^2(g_1) - 1}{2}$$

$$+ b_2 \cdot \cos(g_2) + c_2 \cdot \frac{3 \cdot \cos^2(g_2) - 1}{2}$$

28 $B(g)$ simulates the hot spot with a height B_0 and a width h .
29 Model “Hapke + specular” uses 12 parameters:

$$\{\omega, B_0, h, b_1, c_1, g_1, b_2, c_2, g_2\} + \{A, \alpha, n\}$$

31 Multiple scattering is simulated using the assumption
32 that the surface is lambertian with a reflectance coeffi-
33 cient calculated by the *phase* module. For the Hapke
34 model with $b_2 = c_2 = g_2 = 0$, multiple scattering is cal-
35 culated with:

$$\langle \rho(\Psi_{nv}) \rangle = \frac{1 - (1 - \omega)^{0.5}}{1 + 2 \cdot (1 - \omega)^{0.5} \cdot \cos \Psi_{nv} + \rho_{\text{spe, hd}}(\Omega_v)}$$

- 37 • *Type 3: Functions $T_d(\Omega_s, \Omega_v)$, $T_{\text{spe}}(\Omega_s, \Omega_v)$ and $T_{\text{pol}}(\Omega_s,$
38 $\Omega_v)$ represent the total, specular and polarized reflectance.
39 They can be used with horizontal surfaces only.*

References

- Albinet C (2008) Modélisation 3D des flux et du bilan 41
d’énergie des zones urbaines Modélisation des échanges 42
d’énergie des milieux urbains. M2 report. Paul Sabatier 43
University, Toulouse, France, 57pp 44
- Berk A, Bernstein LS, Robertson DC (1989) MODTRAN: 45
a moderate resolution model for LOWTRAN 7, 46
GL-TR-89-0122, Geophys. Lab., Bedford, MA, USA, 47
38pp 48
- Boyat P (2001) Modélisation du transfert radiatif dans le 49
domaine thermique des surfaces terrestres. Report. École 50
Nationale Supérieure d’Ingénieurs de Constructions 51
Aéronautiques, Toulouse, France, 85pp 52
- Dallest T (2001) Modélisation du transfert radiatif 53
atmosphérique dans le domaine de l’infrarouge thermi- 54
que. École Nationale Supérieure d’Hydraulique et de 55
Mécanique de Grenoble. Report, France, 78pp 56
- Gascon F (2001) Modélisation Physique d’Images de 57
Télétection Optique. PhD Thesis. Université Paul Saba- 58
tier, Toulouse, France 59
- Gastellu-Etchegorry JP, Demarez V, Pinel V, Zagolski F 60
(1996) Modeling radiative transfer in heterogeneous 61
3-D vegetation canopies. Remote Sens Environ 58: 62
131–56 63
- Gastellu-Etchegorry JP, Guillevic P, Zagolski F, Demarez 64
V, Trichon V, Deering D, Leroy M (1999) Modeling 65
BRF and radiation regime of tropical and boreal 66
forests – BRF. Remote Sens Environ 68: 281–316 67
- Gastellu-Etchegorry JP, Gascon F, Estève P (2003) An 68
interpolation procedure for generalizing a look-up table 69
inversion method. Remote Sens Environ 87: 55–71 70
- Gastellu-Etchegorry JP, Martin E, Gascon F (2004) 71
DART: a 3-D model for simulating satellite images 72
and surface radiation budget. Int J Remote Sens 25(1): 73
75–96 74
- Gentine P (2002) Amélioration des images simulées par 75
DART. Report. École Nationale Supérieure de l’ 76
Aéronautique et l’Espace, Toulouse, France, 75pp 77
- Govaerts Y, Verstraete MM (1998) Raytran. A Monte Carlo 78
ray tracing model to compute light scattering in three- 79
dimensional heterogeneous media. IEEE Trans Geosci 80
Remote Sens 36: 493–505 81
- Grau E (2008) DART atmosphere radiative transfer model- 82
ing, 2008 M2 report, CESBIO 83
- Guillevic P, Gastellu-Etchegorry JP (1999) Modeling 84
BRF and radiation regime of tropical and boreal fore- 85
sts – PAR regime. Remote Sens Environ 68: 317–40 86
- Guillevic P, Gastellu-Etchegorry JP, Demarty J, Prévot L 87
(2003) Thermal infrared radiative transfer within three- 88
dimensional vegetation cover, J Geophys Res Atmos 89
ATMOSPH 108(D8); DOI: 10.1029/2002JD002247 90
- Hapke B (1993) Theory of reflectance and emittance spec- 91
troscopy. Cambridge University Press, New York 92
- Jacquemoud S, Baret F, Hanocq JF (1992) Modeling spectral 93
and bidirectional soil reflectance. Remote Sens Environ 94
41: 123–32 95
- Kimes DS, Sellers PJ (1985) Inferring hemispherical reflec- 96
tance of the Earth’s surface for global energy budgets 97

- 1 from remotely sensed nadir or directional radiance values. 43
2 Remote Sens Environ 18: 205–23 44
- 3 Malenovský Z, Martin E, Homolova L, Pokorný R, 45
4 Schaepman ME, Gastellu-Etchegorry J-P, Zurita Milla 46
5 R, Clevers JGPW, Cudlin P (2005) Influence of forest 47
6 canopy structure simulated using the discrete anisotropic 48
7 radiative transfer (DART) model on the retrieval of spruce 49
8 stand LAI. In: 9th International Symposium on Physical 50
9 Measurements and Signatures in Remote Sensing 51
10 (ISPMSRS), Beijing, 17–19 October 2005. Beijing: 52
11 ISPRS WG VII/1, 3pp 53
- 12 Malenovský Z, Ufer C, Lhotakova Z, Clevers JGPW, 54
13 Schaepman ME, Albrechtova J, Cudlin P (2006) A new 55
14 hyperspectral index for chlorophyll estimation of a forest 56
15 canopy: area under curve normalised to maximal band 57
16 depth between 650–725 nm, EARSeL eProceedings, vol. 58
17 5(2), pp. 161–72 59
- 18 Malenovský Z, Martin E, Homolová L, Gastellu-Etchegorry 60
19 J-P, Zurita-Milla R, Schaepman ME, Pokorný R, Clevers 61
20 JGPW, Cudlín P (2008) Influence of woody elements of a 62
21 Norway spruce canopy on nadir reflectance simulated by 63
22 the DART model at very high spatial resolution. Remote 64
23 Sens Environ 112: 1–18 65
- 24 Martin E (2006) DART: Modèle 3D Multispectral et Inver- 66
25 sion d’Images Optiques de Satellite – Application aux 67
26 couverts forestiers. PhD thesis. Paul Sabatier University 68
- 27 Masson V (2000) A physically-based scheme for the urban 69
28 energy budget in atmospheric models. Bound Layer 70
29 Meteorol 94: 357–97 71
- 30 Masson V, Gomes L, Pigeon G, Liousse C, Pont V, 72
31 Lagouarde J-P, Voogt JA, Salmond J, Oke TR, Legain 73
32 D, Garrouste O, Lac C, Connan O, Briottet X, Lachéradé S 74
33 (2007) The canopy and aerosol particles interaction in 75
34 toulouse urban layer (CAPITOU) experiment. Meteorol 76
35 Atmos Phys, this issue 77
- 36 North PRJ (1996) Three-dimensional forest light inter- 78
37 action model using a Monte Carlo method. IEEE 79
38 Trans Geosci Remote Sens 34: 946–56 80
- 39 Pinel V, Gastellu-Etchegorry JP (1998) Sensitivity of tex- 81
40 ture of high resolution images of forest to biophysical 82
41 and acquisition parameters. Remote Sens Environ 65: 83
42 61–85 84
- Pinty B, Gobron N, Widlowski JL, Gerstl SAW, Verstraete 43
MM, Antunes M, Bacour C, Gascon F, Gastellu- 44
Etchegorry JP, Jacquemoud S, North P, Qin W, Thompson 45
R (2001) Radiation transfer model intercomparaison 46
(RAMI) exercise. J Geophys Res 106: D11, 11937–56 47
- Pinty B, Widlowski J-L, Taberner M, Gobron N, Verstraete 48
MM, Disney M, Gascon F, Gastellu J-P, Jiang L, Kuusk A, 49
Lewis P, Li X, Ni-Meister W, Nilson T, North P, Qin W, 50
Su L, Tang S, Thompson R, Verhoef W, Wang H, Wang J, 51
Yan G, Zang H (2004) RAdiation transfer Model Intercom- 52
parison (RAMI) exercise: results from the second phase. J 53
Geophys Res 109: D06210; DOI: 10.1029/2003JD004252 54
- Sillon FX, Arvo JR, Westin SH, Greenberg DP (1991) A 55
global illumination solution for general reflectance dis- 56
tributions. Comput Graph 25: 187–96 57
- Soux CA, Voogt JA, Oke TR (2004) A model to calculate 58
what a remote sensor ‘sees’ of an urban surface. Bound 59
Layer Meteorol 111: 109–32 60
- Thompson RL, Goel NS (1998) Two models for rapidly 61
calculating bidirectional reflectance: Photon spread (Ps) 62
model and statistical photon spread (SPS) model. Remote 63
Sens Rev 16: 157–207 64
- Voogt JA, Oke TR (1998) Effects of urban surface geometry 65
on remotely sensed surface temperature. Int J Remote 66
Sens 19: 895–920 67
- Voogt JA, Oke TR (2003) Thermal remote sensing of urban 68
climates. Remote Sens Environ 86: 370–84 69
- Widlowski JL, Taberner M, Pinty B, Bruniquel-Pinel V, 70
Disney M, Fernandes R, Gastellu-Etchegorry J-P, Gobron 71
N, Kuusk A, Lavergne T, Leblanc S, Lewis PE, Martin E, 72
Mottus M, North PRJ, Qin W, Robustelli M, Rochdi N, 73
Ruiloba R, Soler C, Thompson R, Verhoef W, Verstraete 74
MM, Xie D (2007) The third RAdiation transfer Model 75
Intercomparison (RAMI) exercise: Documenting progress 76
in canopy reflectance models. J Geophys Res 112: 77
D09111; DOI: 10.1029/2006JD007821 78
- Widlowski J-L, Robustelli M, Disney M, Gastellu- 79
Etchegorry J-P, Lavergne T, Lewis P, North PRJ, Pinty 80
B, Thompson R, Verstraete MM (2008) The RAMI On- 81
line Model Checker (ROMC): a web-based benchmarking 82
facility for canopy reflectance models. Remote Sens 83
Environ 112: 1144–50 84